



Enhanced alpha-amylase inhibition activity of amine-terminated PAMAM dendrimer stabilized pure copper-doped magnesium oxide nanoparticles

Jaison Jeevanandam^a, Mara Gonçalves^a, Rita Castro^a, Juan Gallo^b, Manuel Bañobre-López^b, João Rodrigues^{a,c,*}

^a CQM-Centro de Química da Madeira, Universidade da Madeira, Campus da Penteada, 9020-105 Funchal, Portugal

^b Advanced (magnetic) theranostic nanostructures lab (AmTheNa), Nanomedicine group, International Iberian Nanotechnology Laboratory (INL), Braga 4715-330, Portugal

^c School of Materials Science and Engineering, Center for Nano Energy Materials, Northwestern Polytechnical University, Xi'an 710072, China

ARTICLE INFO

Keywords:

MgO nanoparticles
Dendrimers
Dopants
Antidiabetic activity
Alpha-amylase enzyme

ABSTRACT

The present work aims to prepare copper-doped MgO nanoparticles via a sol-gel approach and study their antidiabetic alpha-amylase inhibition activity with undoped MgO nanoparticles. The ability of G5 amine-terminated polyamidoamine (PAMAM) dendrimer for the controlled release of copper-doped MgO nanoparticles to exhibit alpha-amylase inhibition activity was also evaluated. The synthesis of MgO nanoparticles via sol-gel approach and optimization of calcination temperature and time has led to the formation of nanoparticles with different shapes (spherical, hexagonal, and rod-shaped) and a polydispersity in size ranging from 10 to 100 nm with periclase crystalline phase. The presence of copper ions in the MgO nanoparticles has altered their crystallite size, eventually modifying their size, morphology, and surface charge. The efficiency of dendrimer to stabilize spherical copper-doped MgO nanoparticles (ca. 30 %) is higher than in other samples, which was confirmed by UV-Visible, DLS, FTIR, and TEM analysis. The amylase inhibition assay emphasized that the dendrimer nanoparticles stabilization has led to the prolonged enzyme inhibition ability of MgO and copper-doped MgO nanoparticles for up to 24 h.

1. Introduction

In the 21st century, diabetes is one of the life-threatening illnesses among humans, next to cancer [1]. According to International Diabetes Federation (IDF), in 2021, about 537 million people between the ages of 20 and 79 are living with diabetes worldwide [2]. Further, IDF also reported that about one in ten people globally were affected by diabetes and its associated complications. The prediction is that in 2030 about 643 million people will have diabetes, and by the year 2045, around 783 million [3]. Hence, treatment modalities for curing diabetes have gained significant attention among researchers. Type 1 and 2 are the two common diabetes forms caused by either the inability of the pancreas to secrete insulin or the inability of the pancreatic cells to make use of the secreted insulin due to insulin resistance, respectively [4]. In both types, the inhibition of enzymes, such as alpha-amylase and alpha-glucosidase,

delays the carbohydrate breakdown in saliva, small intestine and limits postprandial glucose excursion in the blood [5]. Plant-based compounds are generally used as enzyme inhibitors to delay and reduce postprandial blood glucose excursion [6–8]. Even though these phyto-compounds are beneficial for diabetes treatment, the lack of stability and tedious formulation are the major limitations of these enzyme inhibitors [9,10]. In addition, uncontrolled inhibition of digestive enzymes, especially alpha-amylase, can lead to undigested starch in the large bowel, eventually leading to colonic fermentation, flatulence, gastrointestinal upset, and abdomen distension [11]. Thus, there is a huge demand for a novel drug that can selectively inhibit digestive enzymes without leading to any side effects in the diabetic patients.

Nowadays, nanoparticles are gathering researcher's attention to develop new diagnosis and treatment systems for diabetes [12]. Among these nanoparticles, metal oxide nanoparticles, such as iron oxide,

Abbreviations: IDF, International Diabetes Federation; PAMAM, Poly(amidoamine); Cu-MgO, Copper-doped Magnesium oxide; PDI, Polydispersity index; TG-DTA, Thermogravimetry-differential thermal analysis; SEM, Scanning electron microscope; TEM, Transmission electron microscope; DLS, Dynamic light scattering; XRD, X-ray diffraction; COD, Crystal open database; FTIR, Fourier transform infrared spectroscopy.

* Corresponding author at: CQM-Centro de Química da Madeira, Universidade da Madeira, Campus da Penteada, 9020-105 Funchal, Portugal.

E-mail addresses: joaoc@staff.uma.pt, joaor@uma.pt (J. Rodrigues).

<https://doi.org/10.1016/j.bioadv.2023.213535>

Received 2 January 2023; Received in revised form 16 June 2023; Accepted 19 June 2023

Available online 21 June 2023

2772-9508/© 2023 The Authors. Published by Elsevier B.V. This is an open access article under the CC BY license (<http://creativecommons.org/licenses/by/4.0/>).

copper oxide, lead oxide, magnesium oxide, zinc oxide, and manganese dioxide, either as prepared or functionalized, are under massive research as inhibitors of alpha-amylase and alpha-glucosidase enzyme, respectively [13–19]. It can be noted that compared to other metal oxide nanoparticles, magnesium oxide (MgO) nanoparticles possess enhanced enzyme inhibition ability via reactive oxygen species (ROS) release. This mechanism leads to high thermal and pressure stability, high conductivity, less toxicity toward normal cells, high bioactivity, biocompatibility, and bioavailability [20–22]. Hence, MgO nanoparticles, synthesized either via a physical, chemical, or biological approach, can be used as a potential enzyme inhibitor [23–25]. However, physical synthesis (e.g.: laser ablation) of MgO nanoparticles can lead to stable nanoparticles yet require a high energy source [26], whereas biological synthesis via bacterial, fungal, or plant extract can yield nanoparticles with low toxicity yet low stability [27]. Notably, chemical routes, especially via the sol-gel approach, can yield relatively less toxic MgO nanoparticles with high stability [28]. In addition, the sol-gel approach is simple, cost-effective, requires low reaction temperature, and yields a highly pure final product with a high surface-to-volume ratio and compositional control of the metal oxides [29,30]. However, agglomeration and polydispersity are the major issues in sol-gel synthesized nanoparticles. This issue can be overcome by incorporating metal dopants into the crystal structure, thus obtaining stable monodispersed nanoparticles [31]. Further, adding metal dopants has been proven to alter the crystal structure, eventually enhancing their physicochemical and even biological properties [32].

Even though doped nanoparticles possess enhanced biological properties than the nanoparticle itself, they must be reformulated to be applied for biological applications due to challenges related to bioavailability and targeted delivery [33,34]. Several studies indicated that distinct generations of dendrimers are highly beneficial in the formulation of various nanoparticles for desired biological applications [35–38]. Hence, dendrimers have been identified to be a potential formulation material to contrive metallic nanoparticles or nanomedicines for specific biomedical applications [39,40]. Thus, the present work aims to synthesize metal-doped MgO nanoparticles via a sol-gel approach and compare their antidiabetic alpha-amylase inhibition activity with undoped MgO nanoparticles. Copper was selected in this study as a potential dopant to reduce the defect in the MgO crystal via partial substitution due to its ionic radius (0.073 nm), which is similar to magnesium (0.072 nm) [41–45]. In addition, the ability of amine-terminated polyamidoamine (PAMAM) dendrimer to control the release of copper-doped MgO nanoparticles was, to our knowledge, also investigated for the first time.

2. Experimental procedure

2.1. Materials

Magnesium acetate tetrahydrate (molecular mass = 214.46 g/mol; purity = 99.5 %) as magnesium precursor was procured from Merck® (Portugal), whereas citric acid (molecular mass = 192.13 g/mol; purity = 99.5 %) as gelling agent was purchased from Chem-Lab (Belgium). Further, ethanol (molecular mass = 46.06 g/mol; purity = 96 %) as solvent, copper acetate monohydrate (molecular mass = 199.65 g/mol; purity = 100 %) and copper nitrate 2.5-hydrate (molecular mass = 232.59 g/mol; purity = 99 %) as dopant source was obtained from Riedel-de Haën (Germany). Amine-terminated fifth-generation PAMAM (G5-NH₂-PAMAM) dendrimer suspended in an aqueous medium was obtained from Dendritech® (USA). All the chemicals required for the amylase inhibition assay were obtained from Merck® (Portugal) and Sigma-Aldrich® (Germany).

2.2. Sol-gel synthesis of MgO and Cu-doped MgO nanoparticles

The synthesis procedure of MgO nanoparticles was adopted from our

previous work with certain modifications [46]. An equimolar ratio (final concentration: 1 M) of magnesium precursor [magnesium acetate tetrahydrate; Mg(CH₃COO)₂·4H₂O] and gelling agent [citric acid; C₆H₈O₇] were dissolved separately in the solvent [ethanol; C₂H₅OH]. After dissolution, the citric acid solution was mixed with magnesium acetate to alter its pH from ~7 to 5 and initiate gel formation. The mixture was undisturbed for 3 h for the completion of gel formation, which was later aged for 16 h at room temperature (25 °C) and dried in a hot air oven (Mettler UM 100 oven) at 100 °C for 24 h. The resultant sample was termed as precalcinated magnesium oxide (MgO) powder. Similar procedures were followed for the synthesis of copper-doped magnesium oxide (Cu-doped MgO), where 1, 2, and 3 % (w/w) of dopant source [copper acetate monohydrate; Cu(CH₃COO)₂/copper nitrate 2.5-hydrate; Cu₂H₁₀N₄O₁₇] was mixed in solvent (ethanol) along with magnesium precursor. The resultant doped samples were termed copper-doped magnesium oxide powders. Later, thermogravimetric-differential thermal analysis (TG-DTA) was utilized to select calcination temperature to form MgO/Cu-doped MgO nanoparticles. Hence, the precalcinated powder samples were calcinated at 550, 650, and 750 °C for 2, 3, and 4 h to optimize the calcination procedure using Nabertherm® muffle furnace-L model at a heating rate of 5 °C/min for the formation of MgO and Cu-doped MgO nanoparticles as shown in Fig. 1.

2.3. Characterization of nanoparticle samples

Initially, Thermogravimetry/Differential Thermal Analysis (TG-DTA) technique using a NETZSCH STA 409 PC/PG equipment was utilized to identify the temperature and time of the calcination process. Further, the Dynamic Light Scattering (DLS) and Electrophoretic Light Scattering (ELS) technique (Malvern® Instruments, Zetasizer Nano ZS EN3600, Worcestershire, UK, equipped with a standard 633 nm laser) was used to analyze the samples (100 mg in 10 ml of ultrapure water of pH 6.5–7) for optimizing calcination temperature and time for the formation of MgO and copper-doped MgO nanoparticles. The samples' average particle size, polydispersity index (PDI), and zeta potential were identified for calcination optimization (100 mg of samples in 10 ml of ultrapure water of pH 6.5–7). The physicochemical characteristics of the nanoparticles, such as crystallinity, optical property, functional group, and morphology, were identified via X-Ray Diffractometer (XRD – Bruker® D8 Advance), Ultraviolet-visible (UV-Vis; PerkinElmer® Lambda 35) spectroscopy, Fourier Transform Infrared (FTIR; PerkinElmer® Spectrum Two) spectroscopy, Scanning Electron Microscopy, with Electron Dispersion Spectroscopy (SEM, EDS; Bench SEM Phenom ProX) and Transmission Electron Microscopy (TEM; JEOL JEM 2100 80–100 kV), respectively.

2.4. Stabilization of nanoparticles with amine-terminated PAMAM dendrimers

The stabilization procedure for the controlled release of nanoparticles, followed by Shi et al. (2006) was used in the present work with certain modifications [47]. In this study, MgO/Cu-doped MgO nanoparticles were dispersed in ultrapure water, where the G5-NH₂-PAMAM dendrimer was added (0.5:0.1 ratio mg/ml; 2.4×10^{-4} M) under constant stirring at room temperature (25 °C) for 2 h (optimization of stabilization reaction time and volume of dendrimer was briefly explained in supplementary information section S.7.). The resultant stabilized nanoparticles were characterized using UV-Vis spectroscopy, FTIR, and DLS/ELS analysis. The stabilization efficiency was known by analyzing the absorbance at 292 nm (UV-Vis spectroscopy) of MgO/Cu-doped nanoparticles present in the supernatant and the stabilized samples due to the presence of oxygen [48]. Later, the final product was isolated via the decantation process, where the supernatant is removed. The precipitate was sonicated for 5 min and lyophilized using a Labconco Freeze Zone 4.5-l freeze drier system for further morphology analysis. SEM analysis was used to analyze the morphology of the optimized

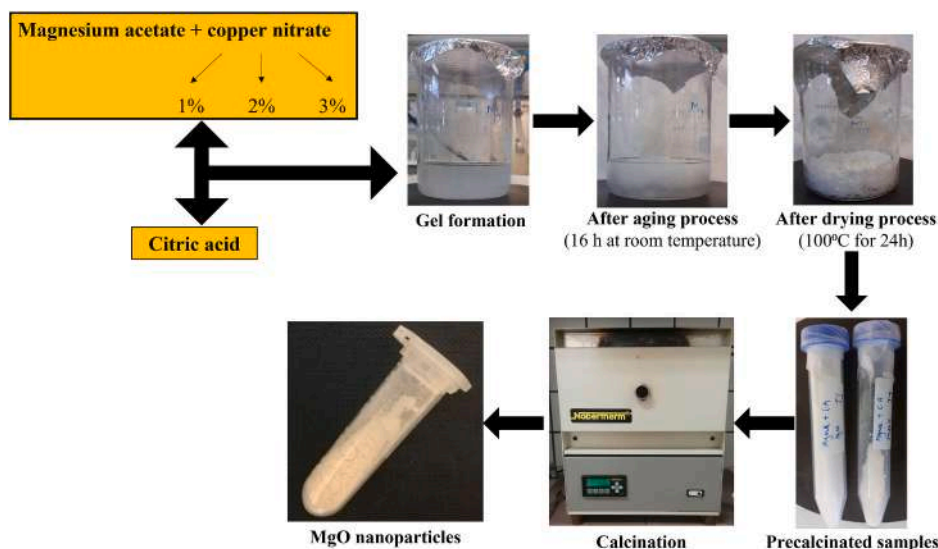


Fig. 1. Sol-gel synthesis approach for MgO nanoparticles and Cu-doped MgO nanoparticle formation.

dendrimer stabilized nanoparticle samples.

2.5. Alpha-amylase inhibition assay

The amylase inhibition activity as described by Ammulu et al. [15] was adopted in the current study with certain modifications. In the present work, the lyophilized alpha-amylase enzyme from human saliva (purchased from Sigma Aldrich®) was applied to identify the alpha-amylase inhibition activity of MgO, Cu-doped MgO, and dendrimer stabilized nanoparticle samples. Initially, the standard maltose graph shown in Fig. 2 was obtained using soluble maltose (2 mg/ml in ultra-pure water). After, 1–5 mg of MgO nanoparticles (spherical) were added to the mixture of starch, sodium chloride, and enzyme to identify the required concentration of nanoparticles for enzyme inhibition. The optical density (OD) value at 520 nm was substituted in the standard maltose graph to determine the concentration of maltose (starch converted into maltose due to enzyme) present in the test samples.

The formula

$$\text{Control} - \text{sample/control} \times 100$$

allowed the calculation of the percentage of enzyme inhibition by the

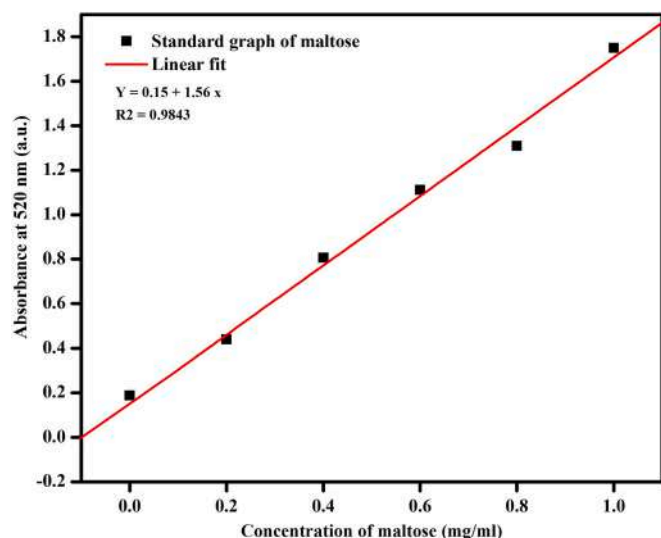


Fig. 2. Standard maltose calibration graph for amylase inhibition activity.

free and dendrimer stabilized nanoparticle samples after 0 and 24 h [15].

3. Results and discussion

It can be noted that the time for gel formation differs between samples due to the addition of different copper dopant sources. Rigid gel formation was observed in undoped samples, whereas the addition of dopants led to fluffy gel formation. The distinct gel formation is an indicator of dopants altering the physical and crystal structure of the precalcinated samples, which was evident from the DLS/ELS and yield analysis as shown in Fig. 3.

While comparing size and PDI (supplementary information, section S.1.), the results as displayed in Fig. 3 (A) denotes that the copper dopant via copper acetate increases the size of the particle and leads to polydispersity and agglomeration, which can be avoided during the calcination process. Further, the hydrodynamic particle size of the samples with copper nitrate as a dopant source is lower compared to copper acetate samples. Furthermore, it can be noted that the copper dopant has increased the particle size, compared to non-doped samples. This shows that the inorganic dopant source (ionic bonds) will lead to lower hydrodynamic particle size, compared to organic precursor (covalent bonds), due to their solubility difference [49]. Although the error bars of the samples are higher due to polydispersity (rapid agglomeration), the PDI of precalcinated MgO is 0.4 (monodispersity with certain agglomeration). In contrast, the PDI of precalcinated Cu-doped MgO sample with copper acetate and copper nitrate as dopant sources is above 0.5 (polydisperse) because of the addition of copper. Further, the error percentage associated with the zeta potential value is also high due to rapid agglomeration [50]. Notably, the addition of a distinct percentage of copper has led to the alteration of precalcinated Cu-doped MgO sample's zeta potential from negative to zero (neutral stability) as indicated in Fig. 3 (B). This denotes that the negative charges due to oxygen presence in precalcinated MgO sample are replaced by the copper ions (positive surface charge) [51,52]. However, the error of the zeta value is also high due to rapid agglomeration, but only for 3 % Cu-doped sample. While using copper nitrate as a dopant source, the surface charge of precalcinated MgO and Cu-doped MgO is below zero (−2.5 to 0 mV range), which indicates that the copper is not doped on the surface. The copper may have replaced the magnesium ions in the crystal via partial substitution, which eventually led to the negative charge of precalcinated MgO sample due to oxygen [45]. This denotes that the negative charge is due to oxygen presence in precalcinated MgO sample,

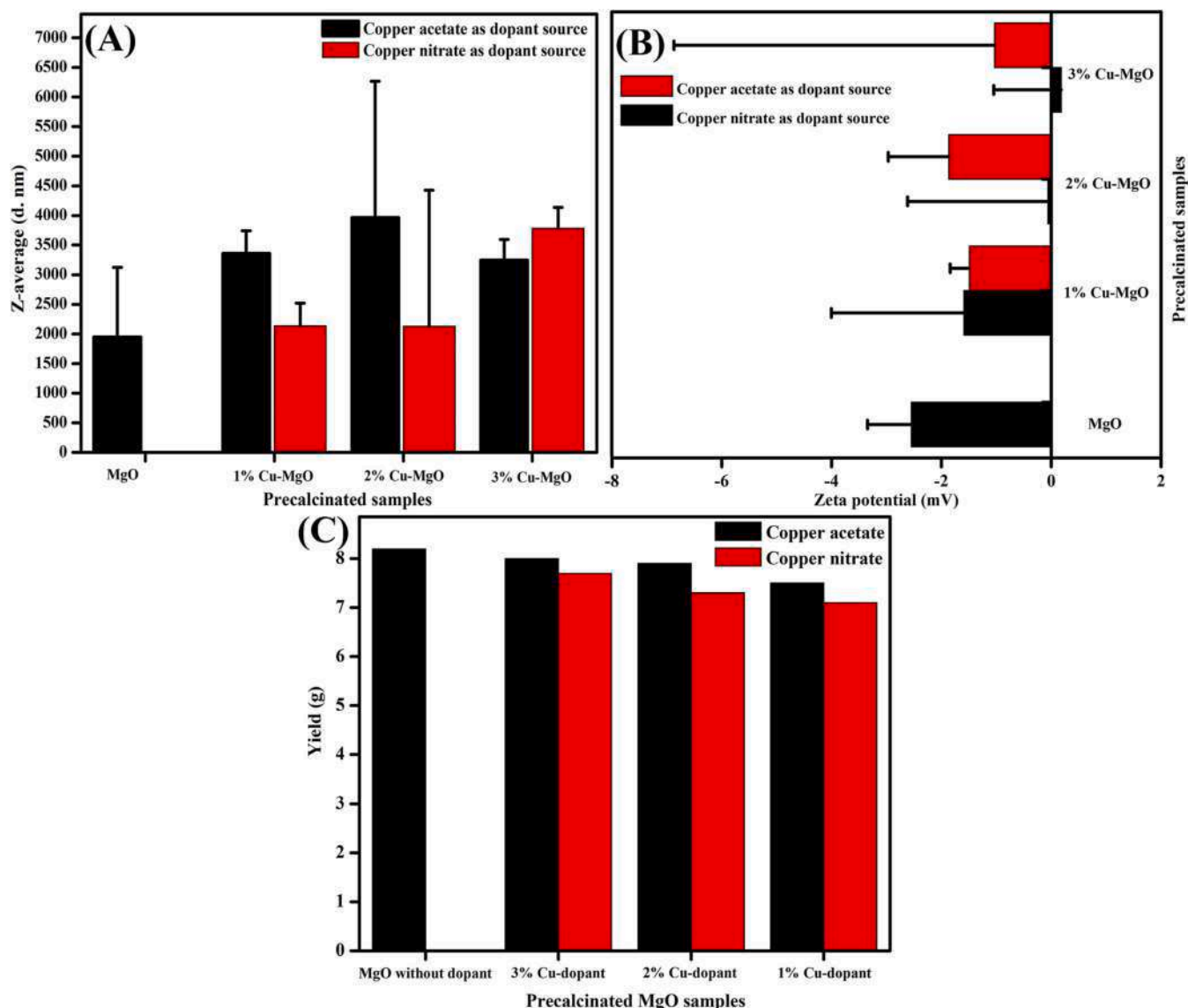


Fig. 3. Characterization of precalculated Cu-doped MgO samples with copper acetate and copper nitrate as dopant sources (A) Average particle hydrodynamic diameter by DLS; (B) Average zeta potential by ELS; and (C) mass yield.

where more Mg ions (smaller ionic radii) are replaced with copper ions (larger ionic radii leading to slightly higher positive surface charge) during the doping process. This process can be attributed to the increase in copper content (due to dopant percentage increase), where the copper ions at the nanoparticle surface may be sub-coordinated to oxide ions and leads to fluctuations in their zeta potential [51,52]. Fig. 3 (C) shows the precalculated samples' yield, indicating that the doping process has reduced the reaction yield. This reduction can be due to the oxygen replacement in the precalculated MgO crystal by copper (copper acetate) or replacing magnesium in the crystal (copper nitrate). In the case of copper acetate, the replacement of a few oxygen atoms via a different percentage of copper (denoted by an increase in zeta potential) may have contributed to the yield reduction. Even though oxygen (atomic mass = 15.9 u) is replaced by copper (atomic mass = 63.5 u), the remaining oxygen forms precalculated MgO like a chain in the gel. In the case of copper nitrate, the magnesium (atomic mass = 24.3 u) ion is replaced by copper, which would have led to the release of magnesium from the crystal core (disrupts crystal form) and are eliminated during the drying process (100 °C for 24 h) along with ethanol as a byproduct. There may be a chance for copper to be present in place of magnesium between gel bonds via partial substitution, which may have reduced the

formation of a few precalculated MgO crystals during gel formation [45,53,54]. Thus, copper nitrate was selected as a dopant source for further analysis as size (size variation gradually increases), PDI (poly-dispersed), and zeta potential (negative charge) are promising compared to copper acetate, even though the yield is slightly lower.

3.1. Thermogravimetry analysis

Fig. 4 (A-D) shows the TG-DTA analysis of precalculated MgO and Cu-doped MgO samples with three degradation stages. The results showed that the crystalline water and carbon dioxide are released in the first thermal degradation stage from ~30–200 °C, whereas the precalculated MgO sample is transformed to MgO nanoparticles in the second thermal degradation stage at ~200–480 °C. It can be noted that between the temperatures ~480–800 °C, there are certain weight losses in the sample, which shows that the calcination at these temperatures can lead to shape modification (comparison table included in supplementary information S.2.9.) [28,55,56]. Above 800 °C, the resultant MgO will be at a stable crystalline state with high thermal stability. Hence, its crystal structure cannot be modified above this temperature. Further, DTA shows that the weight loss and thermal degradation is due

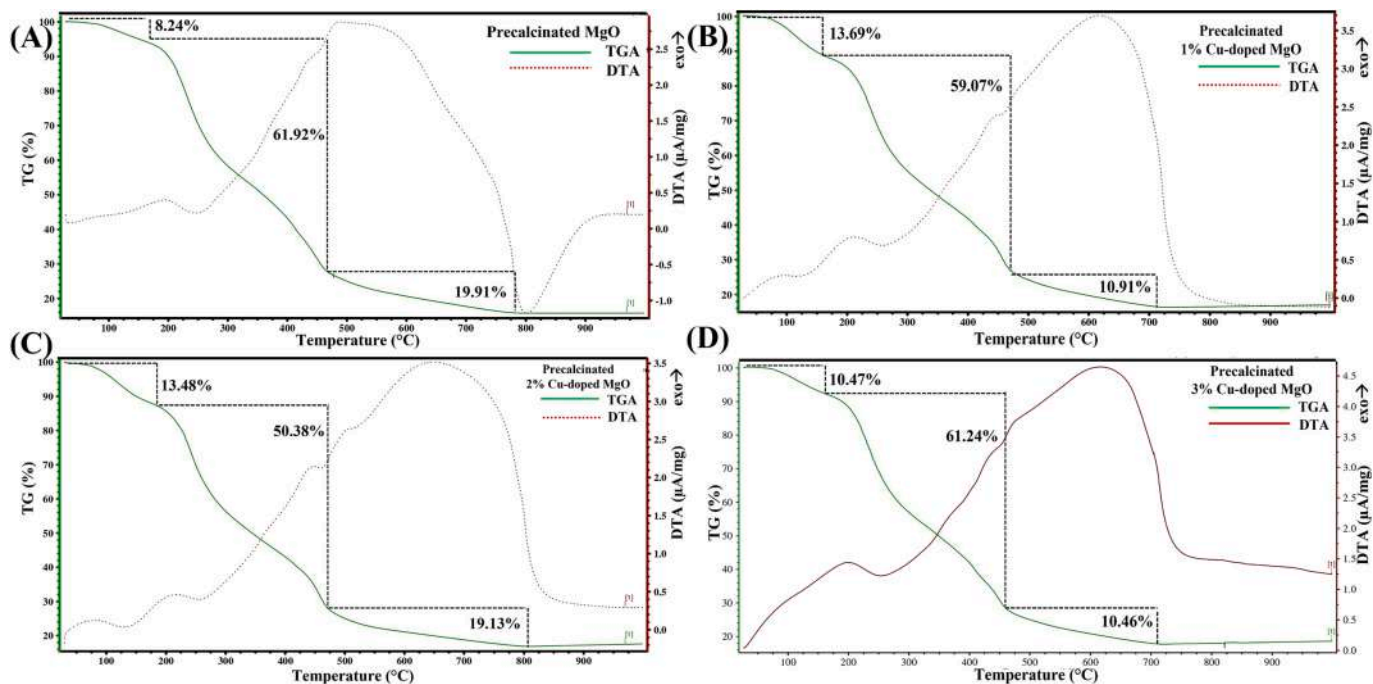


Fig. 4. TG-DTA analysis of precalcinated (A) MgO; (B) 1 % Cu-doped MgO; (C) 2 % Cu-doped MgO and (D) 3 % Cu-doped MgO samples.

to the exothermal reaction, which corresponds to the weight loss. During the third degradation, DTA decreases, indicating that MgO nanoparticles are formed due to weight loss via endothermic reaction. In addition, the difference in weight loss percentage can be attributed to the addition of distinct copper dopant percentages and copper ions in the crystal structure of precalcinated samples [57–59]. Thus, the temperature above 480 °C (2nd degradation) is selected, especially 80–100 °C above second thermal degradation temperature as calcination temperature to alter the shape of nanoparticles [60,61]. The formation of MgO nanoparticles above glass transition temperature has been proven by XRD analysis in Section 3.3. Hence, three distinct temperatures, such as 550, 650, and 750 °C for 2, 3, and 4 h were selected to calcinate the samples for forming nanoparticles with different morphologies.

3.2. DLS/ELS analysis of calcinated samples

Table 1 shows the DLS analysis results (data in supplementary information; section S.2.), which shows the average particle size, PDI, and zeta potential of the calcinated and Cu-doped MgO samples. It is worth noting from the table that the MgO nanoparticles are formed, where the temperature and reaction time plays a significant role in their size, morphology, dispersity, and surface charge [28,62]. Calcinated samples with smaller size, high stability, and PDI below 0.5 were fixed as the criteria for sample selection that can be subjected to further characterization. Accordingly, the selected samples that yielded spherical, hexagonal, and rod-shaped MgO nanoparticles were calcinated at 550 °C for 4 h, 650 °C for 2 h, and 750 °C for 3 h, respectively. Similarly, 1, 2, and 3 % Cu-doped samples calcinated at 550 °C for 2 h, 650 °C for 4 h, and 750 °C for 4 h, respectively, were also selected to yield spherical, hexagonal, and rod-shaped Cu-doped MgO nanoparticles. The comparison between the DLS/ELS data of calcinated MgO and Cu-MgO samples showed that the copper acting as a dopant has reduced the size, and PDI, which eventually increased the stability of the resultant MgO nanoparticles, compared to precalcinated samples [63]. However, the fluctuations in the particle size due to varying dopant concentration, calcination temperature, and time was erratic and further detailed thermodynamic studies must be performed in the future to confirm the influence of these parameters [64,65].

Table 1

DLS/ELS analysis of calcinated MgO and Cu-doped MgO (Cu-MgO) samples.

Calcinated Sample	Calcination temperature and time	Z-average (d. nm)	PDI	Zeta potential (mV)
MgO	550 °C, 2 h	342	0.73	−6.5
	550 °C, 3 h	396.1	0.74	−4.9
	550 °C, 4 h	91.28	0.72	−2.9
	650 °C, 2 h	78.82	0.43	−7
	650 °C, 3 h	91.28	0.35	11.2
	650 °C, 4 h	825	0.32	19.2
	750 °C, 2 h	91.28	0.75	−10.7
	750 °C, 3 h	68.06	0.39	20.5
	750 °C, 4 h	955.4	0.66	−1.4
1 % Cu-MgO	550 °C, 2 h	78.82	0.43	3.8
	550 °C, 3 h	58.77	0.46	18.7
	550 °C, 4 h	122.4	0.51	10
	650 °C, 2 h	531.2	0.51	−8.2
	650 °C, 3 h	122.4	0.72	21.1
	650 °C, 4 h	50.75	0.47	23.6
	750 °C, 2 h	68.06	0.48	−21.8
	750 °C, 3 h	78.82	0.49	17
	750 °C, 4 h	164.2	0.32	16
2 % Cu-MgO	550 °C, 2 h	342	1	−22.9
	550 °C, 3 h	122.4	0.76	18.4
	550 °C, 4 h	1106	0.57	−13.1
	650 °C, 2 h	825	0.90	−18.6
	650 °C, 3 h	58.77	0.65	21
	650 °C, 4 h	68.06	0.37	23.8
	750 °C, 2 h	91.28	0.72	16.3
	750 °C, 3 h	122.4	0.60	20.7
	750 °C, 4 h	91.28	0.37	23.8
3 % Cu-MgO	550 °C, 2 h	78.82	0.46	20.8
	550 °C, 3 h	78.82	0.55	20.3
	550 °C, 4 h	458.7	0.82	−21.4
	650 °C, 2 h	712.4	0.84	13.1
	650 °C, 3 h	68.06	0.31	18.8
	650 °C, 4 h	78.82	0.31	19.8
	750 °C, 2 h	91.28	0.53	22.9
	750 °C, 3 h	105.7	0.27	24.4
	750 °C, 4 h	78.82	0.23	19.6

3.3. Crystallinity analysis

The XRD analysis was utilized to identify the crystallinity of the precalcinated and calcinated MgO samples, as shown in Fig. 5. The XRD data of all the precalcinated samples (Fig. 5 (A) and (B)) showed that the

peaks are not present, which indicated that they are amorphous. However, it can be noted that the calcination process has led to the formation of pure crystalline MgO particles. The XRD analysis of the selected calcinated MgO nanoparticle at 550 °C for 4 h (Fig. 5 (C)) possesses characteristic peaks which are exactly matching with the periclase

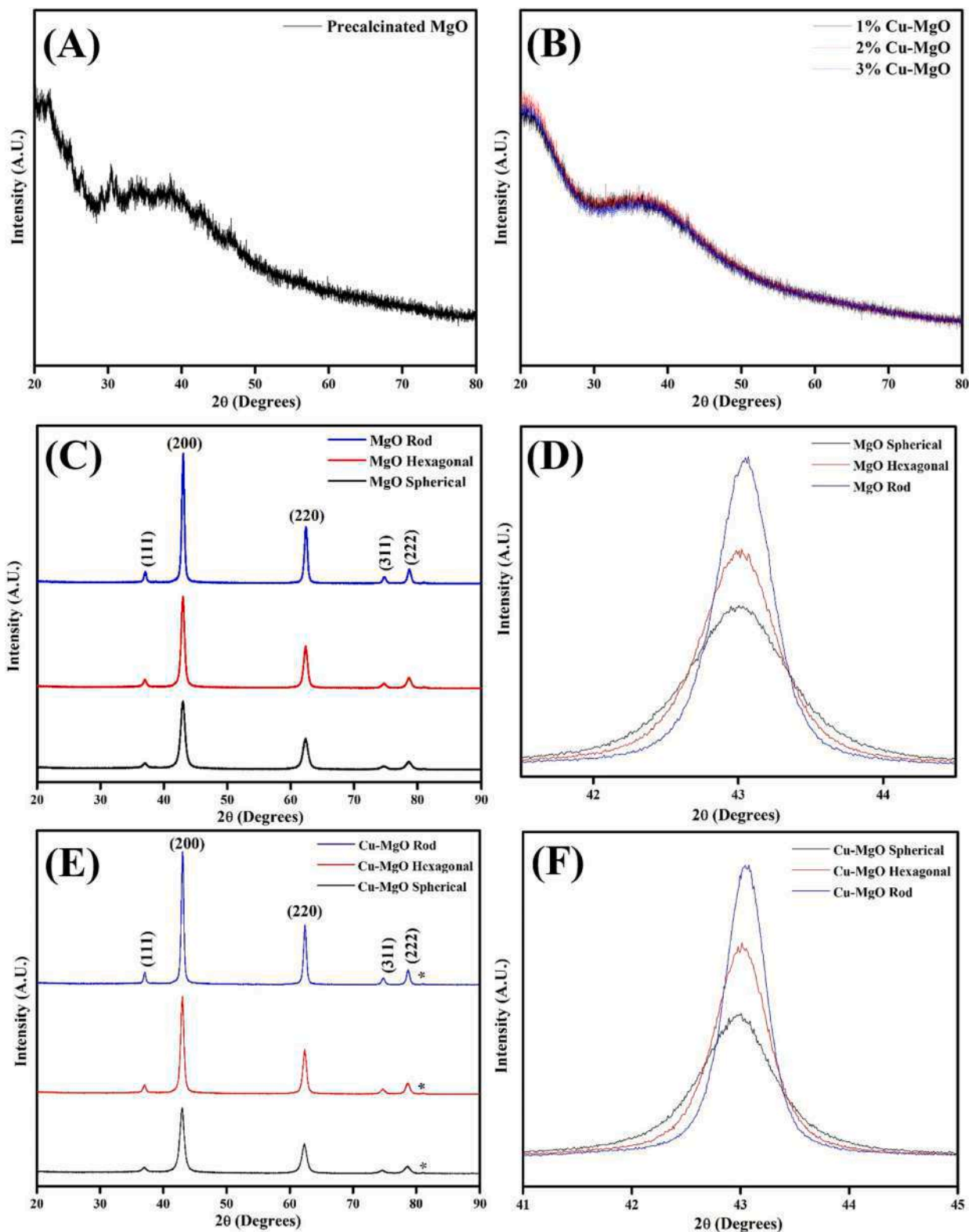


Fig. 5. XRD spectra of (A) precalcinated MgO, (B) precalcinated 1, 2, 3 % of Cu-doped MgO, and (C) calcinated MgO and Cu-doped MgO samples at different temperature leading to distinct (expected) morphology, (D) and (F) Full width of characteristic MgO crystal peak at $2\theta = 42.9^\circ$.

crystalline phase of MgO [COD – crystal open database 00–900-6790; Supplementary information section S.3] [66,67]. The full width half maximum (FWHM) of the samples has been identified (using the non-linear fit of peaks) as 0.9138 at 42.9° of 2 θ . Scherrer's formula has been used to identify the crystallite size of the sample.

$$\text{Scherrer's formula } D = 0.9\lambda/\beta\cos\theta$$

where, 0.9 = Scherrer constant; λ = wavelength of x-rays. In the present study, Bruker X8 XRD equipment was utilized, which uses Cu K α with a wavelength of 1.56 Å; β = FWHM and θ is the corresponding angle of FWHM. An increase in the calcination temperature has led to an increment in the peaks of FWHM. This observation indicates that the calcination has improved the crystallinity and contributed to the shape alteration [68], as Fig. 5 (D) pointed out.

In Cu-doped calcinated samples, there is a minor peak after 80°, which is formed due to the addition of copper ions [69]. Further, it is noteworthy that the XRD peak of Cu-MgO samples (Fig. 5 (E) and (F)) are also similar to MgO (same crystal phase structure) with similar peaks of Cu₂O (cuprous oxide) but with distinct peak intensity [JCPDS 05–0667] [70]. It is evident from the XRD results that there is a minute deflection in the peak position and intensity compared to MgO and COD file data of the reference MgO XRD peak. This confirms that the dopants are present in the sample after calcination and leads to the formation of pure MgO crystals with slight phase modifications [71,72].

The crystallite size calculation using Scherrer's formula showed that the crystals gradually grow concerning the calcination temperature, as listed in Table 2. The MgO sample calcinated at 550 °C possesses 9 ± 0.08 nm of crystallite size, whereas the addition of 1 % copper as a dopant has led to a similar crystallite size (9 ± 0.16 nm). In samples calcinated at 650 °C, the MgO sample possesses 12 ± 0.28 nm of crystallite size, whereas the 2 % copper doping increased their crystallite size (13 ± 0.08 nm). Further, the MgO sample possesses 17 ± 0.05 nm of crystallite size, whereas the 3 % copper doping increased their crystallite size (17 ± 0.23 nm) in samples calcinated at 750 °C. The similar or increased crystallite size in doped samples is due to the morphology transformation, which must have been initiated by the crystal structure change compared to undoped MgO samples [58,73]. The crystallite size of the MgO sample is 9 ± 0.08 nm, whereas the average particle size predicted via DLS analysis is 91.28 nm. As expected, the study emphasized that the crystallite size of all the samples is lower than the DLS values, which refers to the hydrodynamic size. The crystallites together form nanoparticles [74,75], and thus, the result shows that the size of the nanoparticles will be lesser or closer to DLS results due to the interaction of aqueous medium and spherical approximation in DLS analysis [76].

3.4. Functional group analysis

Fig. 6 shows the FTIR spectra of precalcinated and calcinated MgO as well as Cu-doped MgO samples. Table S.4 (A) and (B) in supplementary

material summarize FTIR spectral peaks for comparing the vibrational groups and their respective functional groups present in precalcinated and calcinated samples. The attenuated total reflectance (ATR) method was used to analyze precalcinated MgO samples, whereas the potassium bromide (KBr) method was used to analyze calcinated MgO samples. It is evident that the reflectance property of precalcinated samples is reduced due to the formation of nanosized MgO, where size reduction has led to a difference in their property [77,78]. In precalcinated MgO sample, the presence of O—H group is due to hydroxide [(OH)₂] in the magnesium complex before calcination and C—O group is due to the atmospheric CO₂ absorption by the sample. When compared to calcinated MgO samples, the peak difference at 618 cm^{−1} indicates the presence of hydroxide complex in the material [79,80]. Meanwhile, the presence of O—H and C—O group in MgO sample is due to the absorbance of water and CO₂ from the atmosphere. The characteristic peak at 563 cm^{−1} indicates the presence of Mg—O in the sample [81,82]. Further, the O—H group in precalcinated Cu-doped MgO samples is due to the existence of hydroxide [(OH)₂], while the presence of C—O group is due to the absorption of CO₂ from the atmosphere. The peak difference at ~616 cm^{−1} indicates the influence of copper ions on the hydroxide complex in the precalcinated Cu-doped samples compared to calcinated doped samples [83]. The peak at ca. 850 cm^{−1} represents the presence of magnesium, and the peak at ca. 620 cm^{−1} is due to the presence of hydroxide (precalcinated sample), whereas the peaks at 570 and 420 cm^{−1} represents the oxide in the calcinated sample [46,66]. It is evident that several carboxylic acid peaks which are present in the precalcinated samples are missing in calcinated samples due to the transformation of magnesium complex to MgO. The same trend is also identified in the doped samples. Similarly, a few additional minor peaks are present in doped samples, which is not present in pure MgO samples due to the addition of dopants [84,85]. In addition, the minor peaks can also be due to the oxidation process in the sample, which replaces certain functional groups and shift their position. It can also be noted that certain peaks are missing in undoped and doped samples, indicating the structural difference induced by the doping process in the sample as functional groups [63,86,87]. Thus, it is apparent that the synergistic effect of calcination temperature, time, and dopants can effectively alter the functional groups in the MgO samples, which is evident in the DLS/ELS analysis as variation in the zeta potential, PDI, and average size.

3.5. Morphology analysis of MgO samples

The morphology of the precalcinated samples was analyzed using SEM (without gold sputtering), and elemental analysis was performed using Electron Dispersion Spectroscopy (EDS), as displayed in Fig. 7. The SEM results showed that the precalcinated samples are above 1000 nm in size, which is matching with the DLS results [88]. The EDS results (Fig. 7) revealed the presence of elements such as carbon (probably due to adhesive carbon tape in the sample holder or in the sample), magnesium, and oxygen, in the undoped precalcinated sample. The presence of a reduced atomic percentage of magnesium and more oxygen indicates that the magnesium ion will be in the core of the crystal, where hydrogen and oxygen from the precursor (acetate) are in the edges or interstitial position of the crystal [89,90]. However, the EDS results in Fig. S.5 (A–C) showed that copper was not detected in the metal-doped samples, suggesting that precalcinated samples do not contain copper. The observed morphology changes in the doped samples indicate that the copper ions may have been doped inside the crystal of the precalcinated sample [91]. Further, the fluctuation in the percentage of magnesium and oxygen is due to the polydispersity nature of the precalcinated samples [92,93]. The SEM analysis of the calcinated MgO samples was presented in Supplementary information S.5. It is not possible to view the particles via SEM images as the size of the particles is reduced to nano-regime and also because the MgO, resulting from the conversion of precalcinated magnesium, is an insulator and cannot conduct electrons [94,95]. Thus, TEM analysis was used to identify the

Table 2
Crystallite size of calcinated MgO and Cu-doped MgO samples with standard deviation (SD).

Sample name	Calcination temperature	Calcination time (h)	Doping (%)	Expected morphology	Crystallite size (nm) ± SD
MgO	550 °C	4	–	Spherical	9 ± 0.08
MgO	650 °C	2	–	Hexagonal	12 ± 0.28
MgO	750 °C	3	–	Rod	17 ± 0.05
Cu-MgO	550 °C	2	1	Spherical	9 ± 0.16
Cu-MgO	650 °C	4	2	Hexagonal	13 ± 0.08
Cu-MgO	750 °C	4	3	Rod	17 ± 0.23

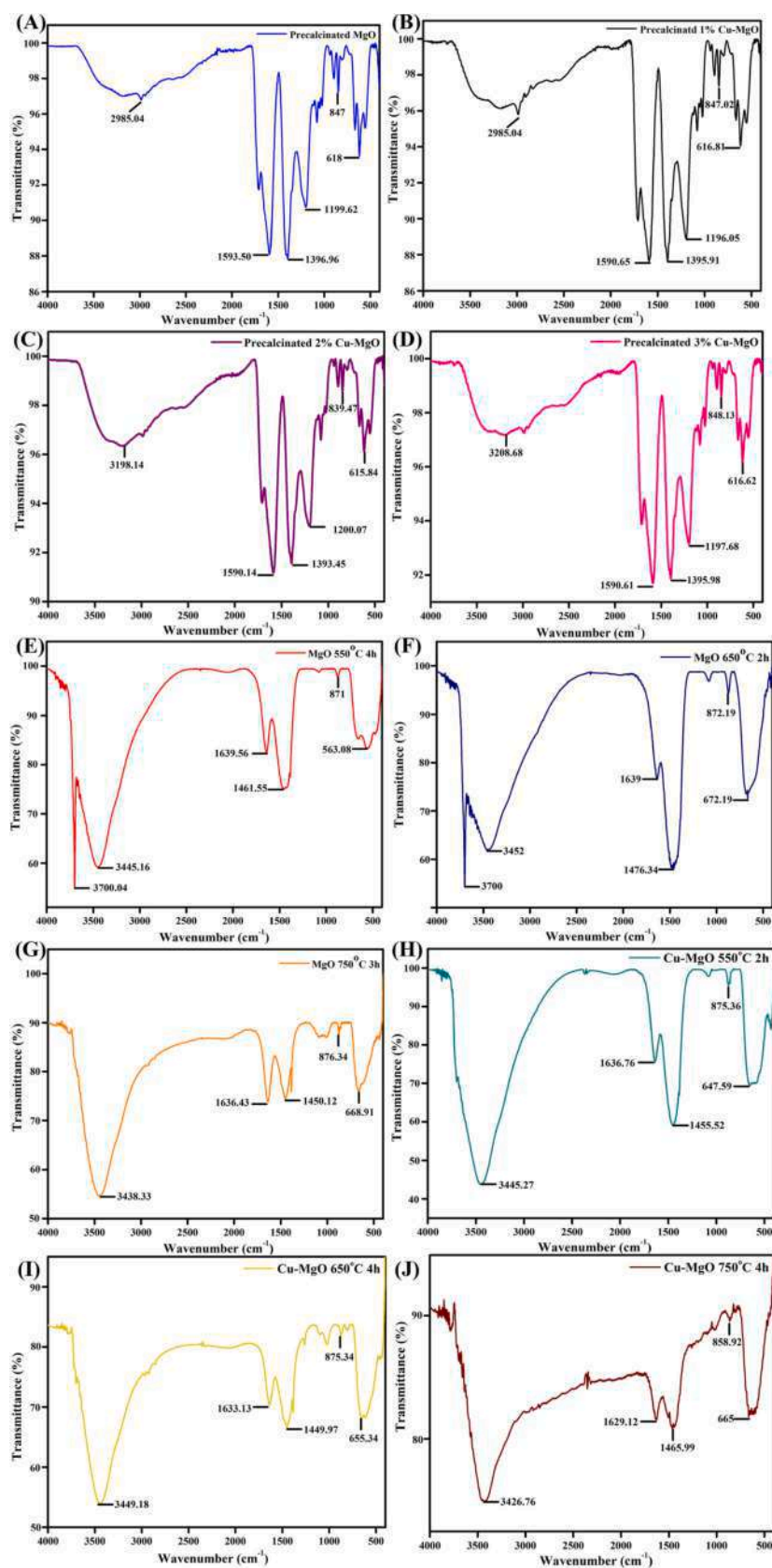


Fig. 6. FTIR spectra of precalcinated (A) MgO, (B) 1 % Cu-doped MgO, (C) 2 % Cu-doped MgO, (D) 3 % Cu-MgO, Calcined (E) MgO at 550 °C, (F) MgO at 650 °C, (G) MgO at 750 °C, (H) 1 % Cu-doped MgO at 550 °C, (I) 2 % Cu-doped MgO at 650 °C and (J) 3 % Cu-doped MgO at 750 °C.

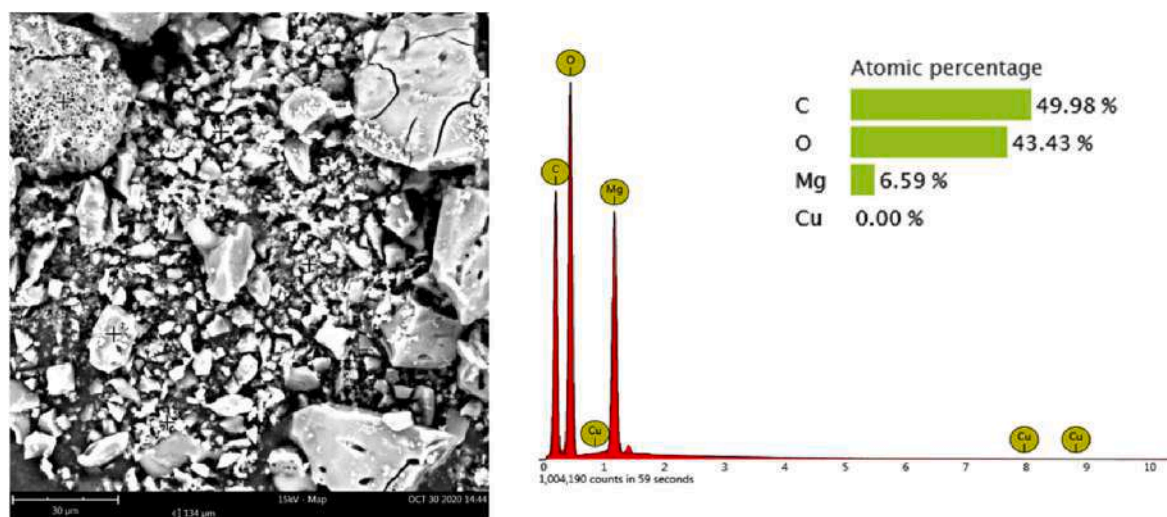


Fig. 7. Scanning electron micrograph and elemental analysis of precalcinated MgO sample (scale = 30 μ m).

morphology of the calcinated samples.

Fig. 8 (A–F) shows the TEM images of calcinated MgO and Cu-doped MgO nanoparticles. The size of the resultant nanoparticles was in the range of ca. 60–100 nm. The shape predicted via DLS and XRD analysis, such as spherical, hexagonal, and rod (elongated hexagon) calcinated at 550, 650, and 750 $^{\circ}$ C is almost similar in most of the samples as indicated by TEM images. Also, the agglomeration indicated by the DLS/ELS analysis also matches the images. The smaller-sized nanoparticles with predicted shapes (transformation from spherical to hexagon to elongated hexagon/rod) has been formed via the influence of calcination temperature, time, and dopant incorporation. However, the shape transformation in copper-doped samples were not evident, especially the rod shape, which may be due to insufficient calcination temperature or time [96]. Further, the solvent used to suspend the samples (ethanol) has led to agglomeration, similar to water. Thus, an alternative solvent or addition of surfactant is required to suspend MgO samples for TEM characterization to provide images without/less agglomeration [46].

3.6. Influence of calcination and dopants on MgO structure

Fig. 9 shows the possible mechanism of the sol-gel process in the formation of MgO and Cu-doped MgO nanoparticles and the influence of dopants and calcination on their morphology. The hydrolysis and condensation process has led to the formation of sol due to pH alteration from 7 (neutral) to 5 (acidic) when the gelling agent citric acid dissolved in ethanol was mixed with the magnesium and dopant precursors dissolved in ethanol [97]. Later, the sol is transformed into wet gel via the aging process, where the elements of precursors, gelling agent, and solvent arrange themselves as a matrix in the gel [98]. Further, the wet gel is allowed to evaporate via the drying process, where the excess ethanol is removed to form xerogel [99]. The xerogel was converted into nanoparticles of spherical, hexagonal, and rod (elongated hexagon) shape via the calcination process, which was confirmed by XRD and TEM analysis. It can be noted that the ionic radius of copper (0.073 nm) is similar to magnesium (0.072 nm), which allows the copper ions to replace magnesium ions of the magnesium complex via partial substitution during the hydrolysis and condensation process to reduce the defects in their amorphous structure [45,100]. The shape difference observed via SEM analysis, elemental analysis using EDS analysis, and crystallite sizes calculated via XRD analysis confirm these attributes, which is due to the replacement of magnesium ions with copper ions of amorphous precalcinated samples [45,101]. Later, the calcination led to the transformation of shapes from spherical to hexagon and hexagon to elongated hexagon and rod [102,103]. The use of FTIR, SEM, and TEM

analysis confirmed that doping with copper and calcination has led to modifications in the morphology of the copper-doped MgO nanoparticles compared to undoped MgO nanoparticles.

3.7. Stabilization efficiency of MgO nanoparticles using PAMAM dendrimers

The MgO nanoparticles synthesized via sol-gel approach are larger \sim 10–100 nm, compared to fifth-generation dendrimers, and thus, amine-terminated fifth-generation PAMAM dendrimer was used as a stabilizing agent for the controlled release of MgO nanoparticles. The standard calibration graph of MgO nanoparticles was obtained via UV-Visible spectroscopy by suspending 10 mg/ml of sample in ultrapure water as shown in supplementary information S.6. Figs. 10 (A) and (B) shows the absorbance of the dendrimer stabilized spherical MgO nanoparticle sample as well as supernatant (free dendrimer/MgO). The characteristic peak at 292 nm indicates the presence of a high concentration of MgO, which was eventually reduced in the supernatant (refer to supplementary information section S.7). In addition, the peak around 280 nm is present only in dendrimer stabilized spherical MgO sample, which may be due to the existence of free dendrimer along with nanoparticles stabilized with dendrimer refer to supplementary information section S.8.1). It is evident from Figs. 10 (C) and (D) that the dendrimer effectively stabilized the spherical and rod/elongated hexagon-shaped copper-doped MgO nanoparticles compared to undoped samples. However, the stabilization efficiency of hexagonal copper doped nanoparticles is less than undoped hexagonal nanoparticles. This observation can be attributed to the doped sample's edge atoms and the presence of copper ions in the MgO crystal's interstitial position, which may have restricted the crucial electrostatic attraction between the dendrimer and the nanoparticle [104–107], as schematically represented in Fig. 10 (E).

3.8. DLS/ELS analysis of PAMAM stabilized MgO nanoparticles samples

The average particle size predicted from DLS analysis showed that the stabilized samples are in the size range of \sim 700–900 nm, as indicated in Table 3. The wide range of particle size with PDI as 1 in supernatant samples indicates the presence of both dendrimer and nanoparticles that are not involved in the stabilization process. The increment in the size is due to the stabilization process. The zeta potential seems to decrease in the dendrimer stabilized samples. The alteration of zeta potential from negative to positive in spherical and hexagonal MgO nanoparticles samples is attributed to the terminal amine functionalization, whereas in rod-shaped MgO sample, the

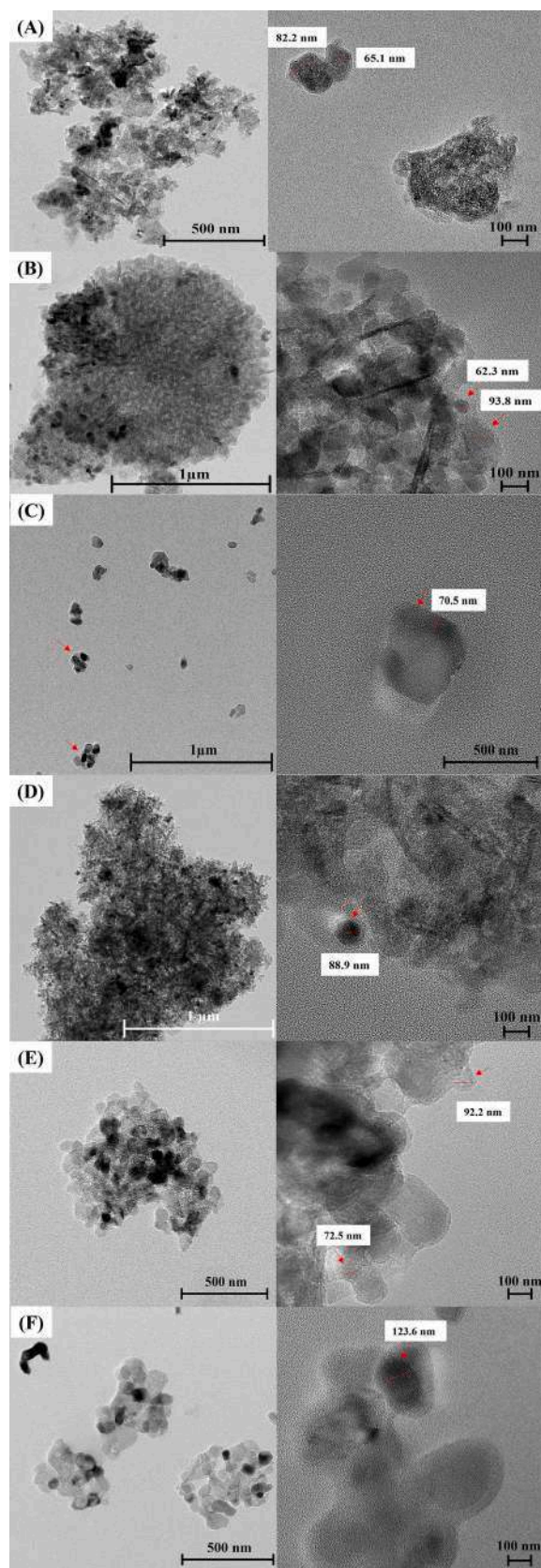


Fig. 8. TEM images in 1 μm /500 nm/100 nm scale of calcinated MgO nanoparticles at (A) 550 $^{\circ}\text{C}$, (B) 650 $^{\circ}\text{C}$, (C) 750 $^{\circ}\text{C}$; (D) 1 % Cu-doped MgO nanoparticles calcinated at 550 $^{\circ}\text{C}$, (E) 2 % Cu-doped MgO nanoparticles calcinated at 650 $^{\circ}\text{C}$ and (F) 3 % Cu-doped MgO nanoparticles calcinated at 750 $^{\circ}\text{C}$.

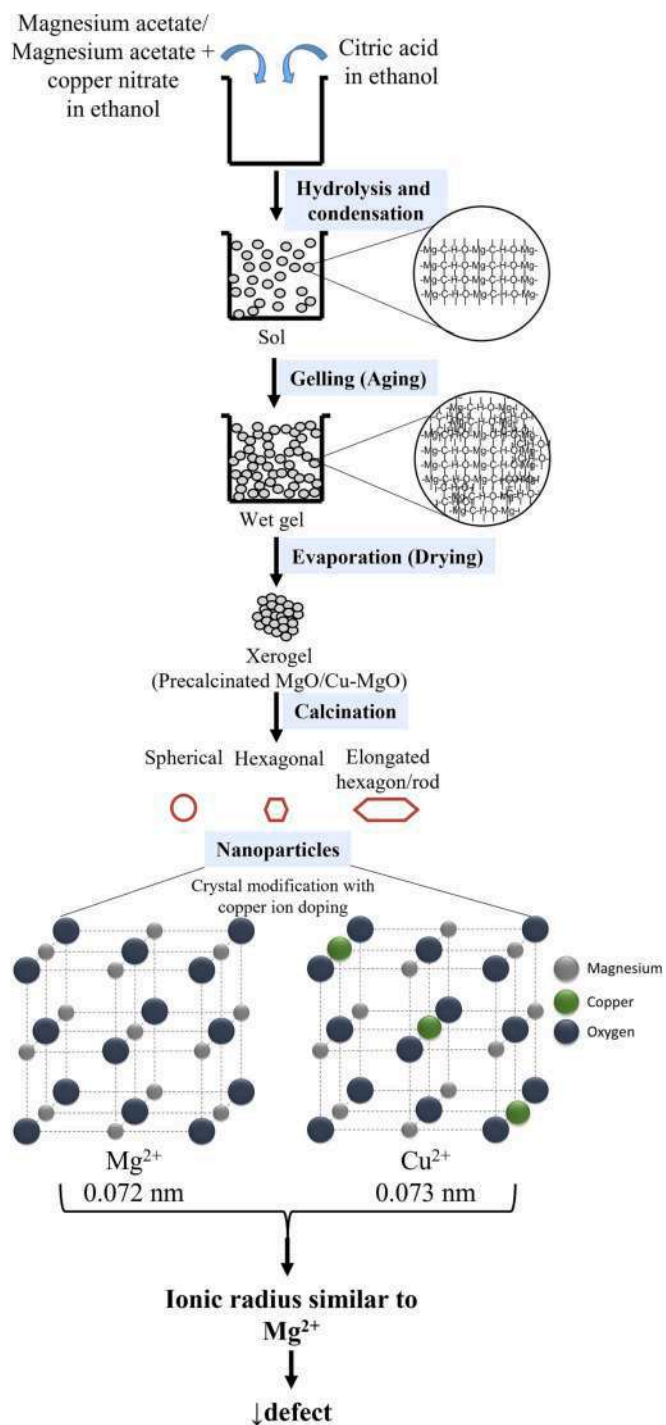


Fig. 9. Possible mechanism of MgO/Cu-doped MgO nanoparticle formation via sol-gel, doping, and calcination process.

positive charge decreases as the negatively charged oxygen group in the MgO nanoparticle is exposed to the surface during stabilization process [108,109]. A similar process (as in rod-shaped MgO) has also been observed in Cu-doped MgO nanoparticle samples. While comparing the data from UV–Visible spectra and DLS analysis, it is evident that the MgO nanoparticles were effectively stabilized by amine-terminated dendrimers (Additional data on optimization of stabilization is presented in supplementary information section S.8.).

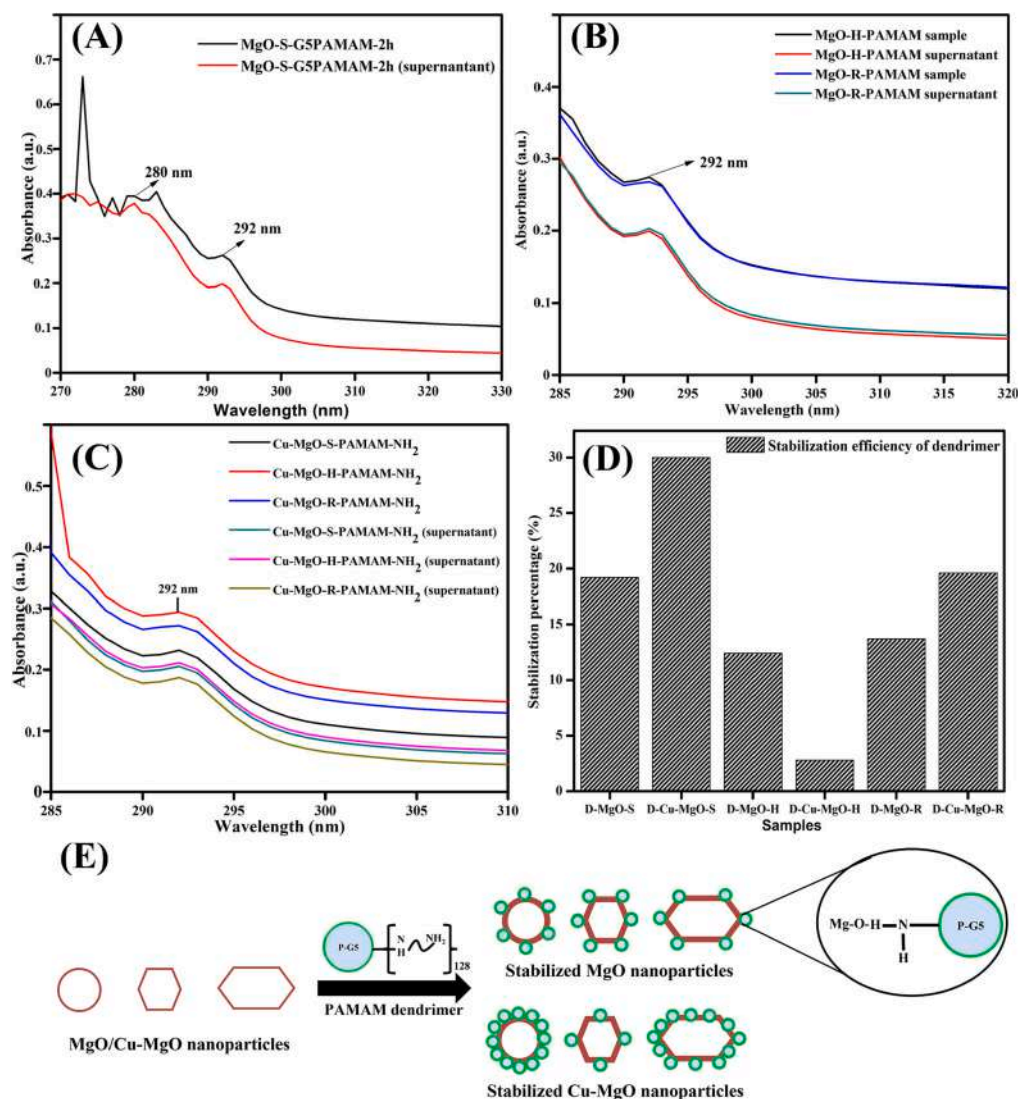


Fig. 10. UV–Visible spectra of G5-PAMAM dendrimer stabilized (A) MgO nanoparticles; (B) hexagonal and rod MgO nanoparticles; (C) Cu-doped MgO nanoparticles; (D) stabilization efficiency of G5-PAMAM dendrimer; (E) Proposed stabilization mechanism of different shapes of MgO nanoparticles with dendrimers. S – spherical, H – hexagon, R – Rod, G5-PAMAM – Fifth generation amine-terminated polyamidoamine dendrimer, D – Dendrimer, Cu – Copper ion as the dopant.

Table 3

Average size, PDI, and zeta potential of MgO, stabilized MgO, Cu-doped MgO, and stabilized Cu-doped MgO nanoparticles.

Sample	Size (d. nm)	Size (d. nm) supernatant	PDI	PDI supernatant	Zeta potential (mV)	Zeta potential (mV) supernatant
MgO-S	91.28		0.725		−2.91	
MgO-S-dendrimer	712.4 and 122.4	1400	0.395	1	12.2	5.69
MgO-H	78.82		0.430		−7	
MgO-H-dendrimer	458.7	1480	0.314	1	13	5.67
MgO-R	68.06		0.399		20.5	
MgO-R-dendrimer	955.4	1100	0.452	1	13.7	6.20
Cu-MgO-S	78.82		0.432		3.83	
Cu-MgO-S-dendrimer	615.1	1154	0.722	0.323	10.6	4.76
Cu-MgO-H	68.06		0.376		23.8	
Cu-MgO-H-dendrimer	966	1066	1	1	15.2	5.45
Cu-MgO-R	78.82		0.239		19.6	
Cu-MgO-R-dendrimer	881.4	6815	0.583	0.849	15.5	6.54

3.9. Functional group analysis of dendrimer stabilized MgO/Cu-doped MgO nanoparticles

The FTIR analysis (Fig. 11 and Table 4) using a KBr method, showed the presence of the primary amine group (NH₂) (3295 cm^{−1}) from the dendrimer and the = O vibrations (2127 cm^{−1}), amides (−CO-NH−)

(1632 cm^{−1}) and 664 cm^{−1} (CH out of plane aromatic band) [110,111]. The variations in these peaks (MgO and Cu-doped MgO) show that certain portions of the MgO are exposed to dendrimer surface even after the stabilization, as indicated by maximum ~30 % stabilization efficiency. Thus, the comparative results of UV–Visible spectra, stabilization efficacy, DLS, and FTIR analysis has led to the selection of spherical

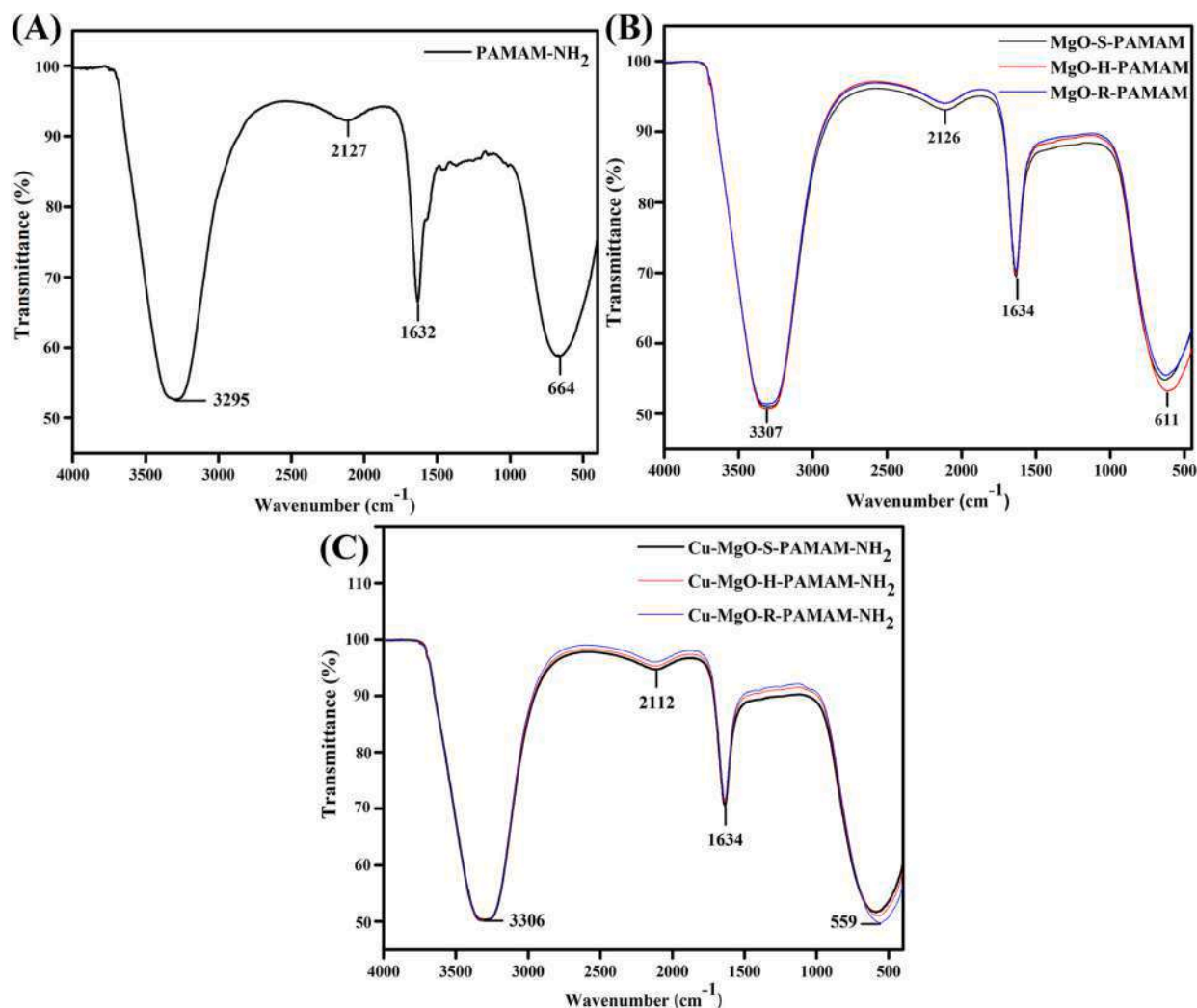


Fig. 11. FTIR spectra of (A) amine-terminated G5-PAMAM dendrimer; (B) different shapes of dendrimer stabilized MgO nanoparticles, and (C) different shapes of dendrimer stabilized Cu-doped MgO nanoparticles. S – Spherical, H – Hexagonal, R – Rod.

Table 4

FTIR spectral peaks of dendrimer stabilized MgO/Cu-doped MgO nanoparticle samples.

Sample	PAMAM	MgO-S-PAMAM	MgO-H-PAMAM	MgO-R-PAMAM
Peak (cm ⁻¹)	3295.00	3307.13	3307.03	3307.29
	2127.00	2126.65	2111.07	2114.94
	1632.08	1634.20	1634.35	1634.31
	664.61	631.44	611.49	619.96

Sample	PAMAM	Cu-MgO-S-PAMAM	Cu-MgO-H-PAMAM	Cu-MgO-R-PAMAM
Peak (cm ⁻¹)	3295.00	3306.71	3307.48	3307.31
	2127.00	2112.01	2122.99	2130.91
	1632.08	1634.29	1634.52	1634.50
	664.61	584.08	571.13	559.55

MgO nanoparticle samples stabilized using amine-functionalized G5-PAMAM dendrimer for further analysis.

3.10. Morphology analysis of dendrimer stabilized MgO/Cu-doped MgO nanoparticles

The SEM analysis, as in Figs. 12 (A) and (B) shows that the

nanoparticles were stabilized by dendrimers. The hollow spaces within the dendrimers (indicated by red arrow mark) represent the presence of MgO nanoparticles, stabilized by dendrimers. Since MgO nanoparticles are insulators or wide bandgap semiconductors and are smaller, it is impossible to view them via a 20- μ m SEM scale. However, the stabilization of nanoparticles via dendrimers was clearly visible with larger size and agglomeration, which matches the DLS analysis.

3.11. Amylase inhibition activity of selected dendrimer stabilized MgO nanoparticle samples

Fig. 13(A) shows the alpha-amylase enzyme inhibition activity of free and PAMAM dendrimer stabilized MgO nanoparticles after 0 and 24 h. It can be noted that the 1 and 2 mg of nanoparticles yielded more maltose than the control samples (without MgO), which may be due to the catalytic effect of the enzyme under MgO influence. On the other hand, 3–4 mg of MgO nanoparticles promoted the inhibition of the alpha-amylase enzyme. In comparison, due to the agglomeration of nanoparticles, a 5 mg sample showed a higher enzymatic catalytic activity [112] (data in supplementary information section S.9). Hence, 3 mg of nanoparticles was selected for further enzyme inhibition analysis.

The results showed that non-stabilized MgO and metal-doped MgO possess a low alpha-amylase inhibition activity compared to the dendrimer stabilized samples at 0 h. Among the non-stabilized samples,

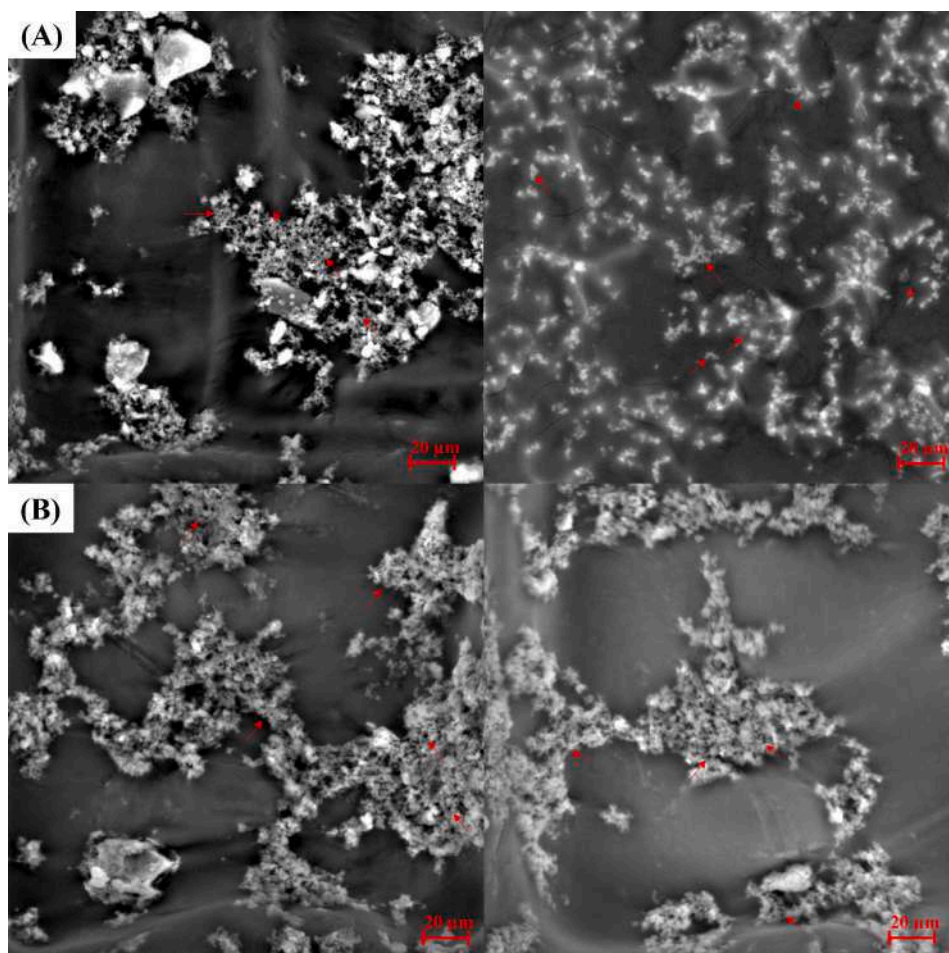


Fig. 12. Scanning electron micrograph of selected (A) G5 amine-terminated PAMAM dendrimer stabilized spherical MgO nanoparticles and (B) G5 amine-terminated PAMAM dendrimer stabilized spherical Cu-doped MgO nanoparticles.

MgO nanoparticles showed high enzyme inhibition activity due to reactive oxygen species (ROS) release. In contrast, Cu-doped MgO samples reduced the inhibition activity, where the copper ions acted as a catalyst to improve the amylase activity and convert starch to maltose [113,114]. It can be noted that the dendrimer stabilized samples showed enhanced enzyme inhibition activity compared to non-stabilized samples. This can be attributed to the amine group of the dendrimer (positive surface charge from DLS/ELS analysis), which may have been attached to the negatively charged site of the enzyme to release nanoparticles, eventually releasing ROS on the target site, inhibiting enzyme activity as proposed in Fig. 13 (B) [115–117]. The alpha-amylase inhibition activity of the non-stabilized and stabilized samples after 24 h shows that the inhibition activity of non-stabilized samples depends on the controlled release of ROS through stabilized NPs. The enzyme inhibition activity of the non-stabilized samples was improved after 24 h, whereas the dendrimer stabilized samples reduced the inhibition after 24 h. This shows that the release of ROS by the nanoparticles is controlled by the dendrimer-mediated stabilization and can be useful in prolonged inhibition of amylase enzyme [118,119].

Several previous studies have confirmed the amylase inhibition property of MgO nanoparticles [120,121]. These studies showed the immediate inhibition response of the nanoparticles by comparing them with commercial enzyme inhibitors named acarbose or metformin. It is worthy to note that the results of enzyme inhibition activity of the dendrimer stabilized MgO nanoparticles demonstrated in the present study is almost on par with the acarbose results and better than the MgO nanoparticle results from previous studies [121,122]. Further, D'Souza et al. [123] prepared zinc-doped MgO nanoparticles using the fruit

extract of *Vateria indica*. The study emphasized that the metal-doped nanoparticles possess enhanced enzyme inhibition efficacy compared to undoped MgO samples. The results in the present study are proximate to the previously reported for free MgO and Cu-doped nanoparticles at 0 h. The stabilization of nanoparticles with G5-amine-terminated PAMAM dendrimer is a major significance of this study, which eventually delays enzyme inhibition activity of nanoparticles at 0 h. Hence, it is evident from the results that the dendrimer enhances the amylase enzyme inhibition of MgO nanoparticles via controlled release and prolonged ROS effect for up to 24 h, when compared to free MgO nanoparticles. This could be beneficial in the long-term for controlled inhibition of amylase without rapidly increasing undigested starch in the intestine of diabetic patients. Although the effect of shape on the biological properties was not evaluated in this study, the presented results show that this aspect deserves to be considered in future studies.

4. Conclusion

In this study, MgO and Cu-doped MgO nanoparticles were synthesized via sol-gel by optimization of calcination temperature and time approach. The nanoparticles' morphology and physicochemical properties were evaluated via a systematic characterization approach (e.g. SEM and TEM). Pure MgO and Cu-doped MgO nanoparticles were prepared in spherical, hexagonal, and rod/elongated rod shapes after the calcination process. Later, the fifth generation, amine-terminated PAMAM dendrimer suspended in an aqueous medium was selected for the stabilization of both MgO and Cu-doped MgO nanoparticles of distinct morphology. The efficiency of the dendrimer to stabilize

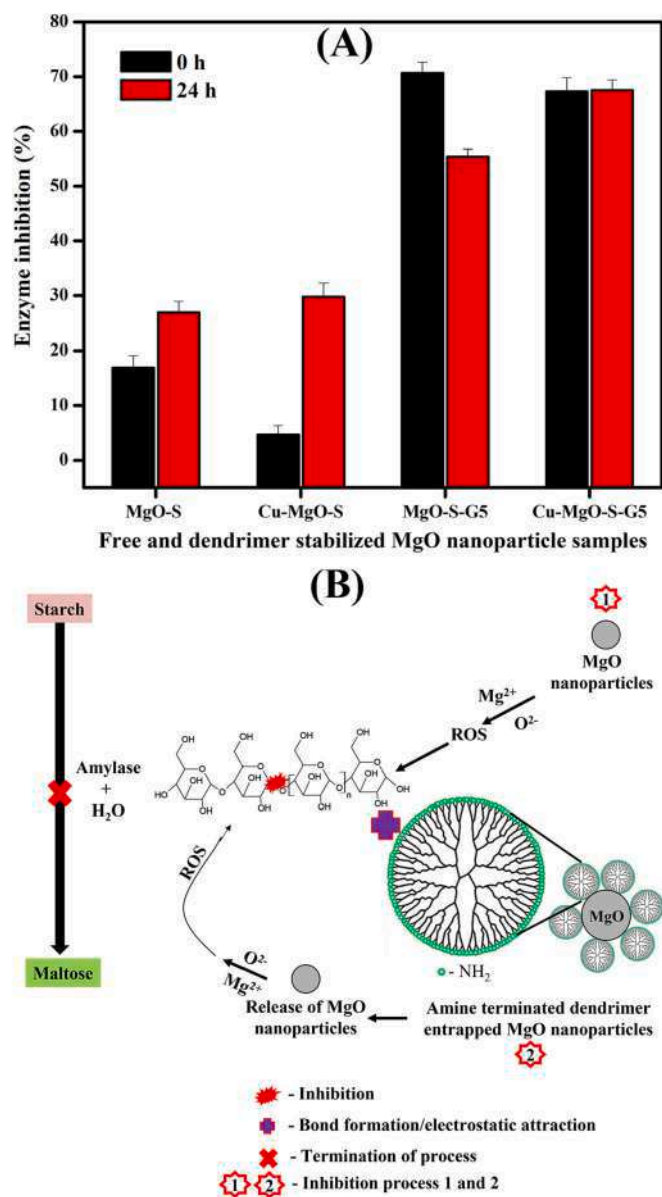


Fig. 13. (A) Alpha-amylase enzyme inhibition activity of free and PAMAM dendrimer stabilized MgO nanoparticles after 0 and 24 h; and (B) Proposed mechanism of alpha-amylase enzyme inhibition.

spherical copper-doped MgO nanoparticles (~30 %) is higher than in the other samples, which was confirmed by UV-Visible spectra, DLS, FTIR, and TEM analysis. The alpha-amylase inhibition assay emphasized that the dendrimer stabilization has prolonged the enzyme inhibition ability of MgO nanoparticles for up to 24 h.

This study will be a benchmark attempt to utilize dendrimer stabilized MgO nanoparticles for antidiabetic studies, especially for digestive enzyme inhibition. Further, this study can be extended to identify the potential of dendrimer formulation for inhibiting other enzymes with antidiabetic efficacy, compared with commercial enzyme inhibitors, other dendrimer generations with distinct functionalization units, and MgO nanoparticles doped with different metal ions.

Declaration of competing interest

The authors declare that they have no known competing financial interests or personal relationships that could have appeared to influence the work reported in this paper.

Data availability

Data will be made available on request.

Acknowledgment

This work was supported by FCT-Fundação para a Ciência e a Tecnologia through the CQM Base Fund - UIDB/00674/2020, by ARDITI-Agência Regional para o Desenvolvimento da Investigação Tecnológica e Inovação, through the project, M1420-01-0145-FEDER-000005 - Centro de Química da Madeira - CQM⁺ (Madeira 14-20 Program). The authors acknowledge Laboratório Regional de Engenharia Civil (LREC), Madeira, Portugal, and Mr. Énio Fernandes (Assistant Technician) for their support to access TG-DTA and XRD equipment. The author (J. R.) acknowledges Programa de Cooperación Territorial INTERREG V-A MAC 2014-2020, Project Inv2Mac (MAC2/4.6d/229) for financial support, including a Post-Doc Grant for J.J. The author (R. C.) acknowledges ARDITI for the support under the scope of Project M1420-09-5369-FSE-000002, through a Post-Doc Grant.

Appendix A. Supplementary data

Supplementary data to this article can be found online at <https://doi.org/10.1016/j.bioadv.2023.213535>.

References

- [1] M.K. Danquah, J. Jeevanandam, Chapter 1 - the current state of diabetes treatment, in: M.K. Danquah, J. Jeevanandam (Eds.), *Emerging Nanomedicines for Diabetes Mellitus Therapeutics*, Elsevier, 2022, pp. 1–31.
- [2] K. Ogurtsova, L. Guariguata, N.C. Barengo, P.L.-D. Ruiz, J.W. Sacre, S. Karuranga, H. Sun, E.J. Boyko, D.J. Magliano, *Diabetes Res. Clin. Pract.* 183 (2022), 109118.
- [3] G.D. Ogle, S. James, D. Dabelea, C. Pihoker, J. Svensson, J. Maniam, E. L. Klatman, C.C. Patterson, *Diabetes Res. Clin. Pract.* 183 (2022), 109083.
- [4] G. Roglic, S.L. Norris, *Ann. Intern. Med.* 169 (2018) 394–397.
- [5] H. Mechchate, I. Es-Safi, A. Louba, A.S. Alqahtani, F.A. Nasr, O.M. Noman, M. Farooq, M.S. Alharbi, A. Alqahtani, A. Bari, *Molecules* 26 (2021) 293.
- [6] G. Grant, M. Duncan, R. Alonso, F. Marzo, Peas and lentils, in: B. Caballero (Ed.), *Encyclopedia of Food Sciences and Nutrition* (Second Edition), Academic Press, Oxford, 2003, pp. 4433–4440.
- [7] P.M. Sales, P.M. Souza, L.A. Simeoni, D. Silveira, *J. Pharm. Pharm. Sci.* 15 (2012) 141–183.
- [8] L. Gong, D. Feng, T. Wang, Y. Ren, Y. Liu, J. Wang, *Food Sci. Nutr.* 8 (2020) 6320–6337.
- [9] X. Nie, Z. Chen, L. Pang, L. Wang, H. Jiang, Y. Chen, Z. Zhang, C. Fu, B. Ren, J. Zhang, *Int. J. Nanomedicine* 15 (2020) 10215.
- [10] N. Sayed, A. Khurana, C. Godugu, *J. Drug Delivery Sci. Technol.* 53 (2019), 101201.
- [11] Y. Dong, B. Zhang, W. Sun, Y. Xing, Chapter 36 - intervention of prediabetes by flavonoids from *Oroxylum indicum*, in: R.R. Watson, V.R. Preedy (Eds.), *Bioactive Food as Dietary Interventions for Diabetes* (Second Edition), Academic Press, 2019, pp. 559–575.
- [12] M.K. Danquah, J. Jeevanandam, Chapter 5 - metal and metal oxide nanoparticles: synthesis, properties, and applications as nanomedicines for diabetes treatment, in: M.K. Danquah, J. Jeevanandam (Eds.), *Emerging Nanomedicines for Diabetes Mellitus Therapeutics*, Elsevier, 2022, pp. 111–142.
- [13] J. Iqbal, A. Andleeb, H. Ashraf, B. Meer, A. Mehmood, H. Jan, G. Zaman, M. Nadeem, S. Drouet, H. Fazal, *RSC Adv.* 12 (2022) 14069–14083.
- [14] B.A. Abbasi, J. Iqbal, T. Mahmood, A. Qyyum, S. Kanwal, *Appl. Organomet. Chem.* 33 (2019), e4947.
- [15] M.A. Ammulu, K. Vinay Viswanath, A.K. Giduturi, P.K. Vemuri, U. Mangamuri, S. Poda, *J. Genet. Eng. Biotechnol.* 19 (2021) 1–18.
- [16] W. Muhammad, M.A. Khan, M. Nazir, A. Siddiquah, S. Mushtaq, S.S. Hashmi, B. H. Abbas, *Mater. Sci. Eng. C* 103 (2019), 109740.
- [17] M.D. Jayappa, C.K. Ramaiah, M.A.P. Kumar, D. Suresh, A. Prabhu, R.P. Devasya, S. Sheikh, *Appl. Nanosci.* 10 (2020) 3057–3074.
- [18] M. Shi, Y. Cen, G. Xu, F. Wei, X. Xu, X. Cheng, Y. Chai, M. Sohail, Q. Hu, *Anal. Chim. Acta* 1077 (2019) 225–231.
- [19] S. Dessai, M. Ayyanar, S. Amalraj, P. Khanal, S. Vijayakumar, N. Gurav, N. Rarokar, M. Kalaskar, S. Nadaf, S. Gurav, *Mater. Lett.* 311 (2022) 131639.
- [20] Y. He, S. Ingudam, S. Reed, A. Gehring, T.P. Strobaugh, P. Irwin, *J. Nanobiotechnol.* 14 (2016) 1–9.
- [21] M.A. Khan, F. Ali, S. Faisal, M. Rizwan, Z. Hussain, N. Zaman, Z. Afsheen, M. N. Uddin, N. Bibi, Saudi, *J. Biol. Sci.* 28 (2021) 5157–5167.
- [22] M.K. Patel, M. Zafaryab, M. Rizvi, V.V. Agrawal, Z.A. Ansari, B.D. Malhotra, S. G. Ansari, *J. Nanoeng. Nanomanuf.* 3 (2013) 162–166.
- [23] J. Jeevanandam, Y.S. Chan, M.K. Danquah, *New J. Chem.* 41 (2017) 2800–2814.
- [24] N.A. Abdulkhaleq, U.M. Nayef, A.K.H. Albarazanchi, *Optik* 212 (2020), 164793.

- [25] K.G. Rao, C.H. Ashok, K.V. Rao, C.S. Chakra, *Int. J. Sci. Res.* 3 (2014) 43–46.
- [26] H. Pereira, C.G. Moura, G. Miranda, F.S. Silva, *Opt. Laser Technol.* 142 (2021), 107181.
- [27] J. Jeevanandam, Y.S. Chan, M.K. Danquah, *ChemBioEng Rev.* 3 (2016) 55–67.
- [28] J. Jeevanandam, Y.S. Chan, M.K. Danquah, *Prot. Met. Phys. Chem. Surf.* 55 (2019) 288–301.
- [29] A.E. Danks, S.R. Hall, Z. Schnepp, *Mater. Horiz.* 3 (2016) 91–112.
- [30] M. Parashar, V.K. Shukla, R. Singh, *J. Mater. Sci. Mater. Electron.* 31 (2020) 3729–3749.
- [31] A. Kumar, N. Yadav, M. Bhatt, N.K. Mishra, P. Chaudhary, R. Singh, *Res. J. Chem. Sci.*, ISSN 2231 (2015) 606X.
- [32] M.V. Zdorovets, A.L. Kozlovskiy, *Vacuum* 168 (2019), 108838.
- [33] D. Khiev, Z.A. Mohamed, R. Vichare, R. Paulson, S. Bhatia, S. Mohapatra, G. P. Lobo, M. Valapala, N. Kerur, C.L. Passaglia, *Nanomaterials* 11 (2021) 173.
- [34] J. Panda, B.S. Satapathy, S. Majumder, R. Sarkar, B. Mukherjee, B. Tudu, *J. Magn. Magn. Mater.* 485 (2019) 165–173.
- [35] C.S. Camacho, M. Urgellés, H. Tomás, F. Lahoz, J. Rodrigues, *J. Mater. Chem. B* 8 (2020) 10314–10326.
- [36] I. Martins, H. Tomás, F. Lahoz, J. Rodrigues, *Biomacromolecules* 22 (2021) 2436–2450.
- [37] C. Camacho, H. Tomás, J. Rodrigues, *Molecules* 26 (2021).
- [38] S. Xiao, R. Castro, J. Rodrigues, X. Shi, H. Tomás, *J. Biomed. Nanotechnol.* 11 (2015) 1370–1384.
- [39] S. Mignani, J. Rodrigues, H. Tomas, R. Roy, X. Shi, J.-P. Majoral, *Adv. Drug Deliv. Rev.* 136–137 (2018) 73–81.
- [40] S. Mignani, J. Rodrigues, H. Tomas, A.-M. Caminade, R. Laurent, X. Shi, J.-P. Majoral, *Sci. China Mater.* 61 (2018) 1367–1386.
- [41] D.-M. Kim, S.-C. Jung, S. Ha, Y. Kim, Y. Park, J.H. Ryu, Y.-K. Han, K.T. Lee, *Chem. Mater.* 30 (2018) 3199–3203.
- [42] M. Ahmad, A.R.A. Usman, S.S. Lee, S.-C. Kim, J.-H. Joo, J.E. Yang, Y.S. Ok, *J. Ind. Eng. Chem.* 18 (2012) 198–204.
- [43] N.G. Schmahl, J. Barthel, G.F. Eikerling, *Z. Anorg. Allg. Chem.* 332 (1964) 230–237.
- [44] M. Paranthaman, K.A. David, T.B. Lindemer, *Mater. Res. Bull.* 32 (1997) 165–173.
- [45] B. Clavier, T. Baptiste, Z. Barbieriková, T. Hajdu, A. Guet, F. Boucher, V. Brezová, C. Roques, G. Corbel, *Mater. Sci. Eng. C* 123 (2021), 111997.
- [46] J. Jeevanandam, Y.S. Chan, M.K. Danquah, *ChemistrySelect* 2 (2017) 10393–10404.
- [47] X. Shi, K. Sun, L.P. Balogh, J.R. Baker, *Nanotechnology* 17 (2006) 4554.
- [48] X. Fuku, N. Matinise, M. Masikini, K. Kasinathan, M. Maaza, *Mater. Res. Bull.* 97 (2018) 457–465.
- [49] A. Seidell, *J. Am. Med. Assoc.* 91 (1928) 1131–1132.
- [50] S. Bhattacharjee, *J. Control. Release* 235 (2016) 337–351.
- [51] J. Jaison, S. Balakumar, Y. Chan, *IOP Conference Series: Materials Science and Engineering*, IOP Publishing, 2015, p. 012005.
- [52] S. Mianxince, B. Liang, Z. Tianliang, Z. Xiaoyong, *J. Rare Earths* 26 (2008) 693–699.
- [53] N. Aboulfotouh, Y. Elbasha, M. Ibrahim, M. Elok, *Ceram. Int.* 40 (2014) 10395–10399.
- [54] M. Sahu, P. Biswas, *Nanoscale Res. Lett.* 6 (2011) 1–14.
- [55] J. Jaison, S. Balakumar, Y.S. Chan, *IOP Publishing*, 2015, pp. 012005.
- [56] J. Jeevanandam, Y.S. Chan, M.K. Danquah, *ChemistrySelect* 2 (2017) 10393–10404.
- [57] M.A. Morsi, S.A. El-Khodary, A. Rajeh, *Phys. B* 539 (2018) 88–96.
- [58] T. Dippong, E.A. Leve, I.G. Deac, E. Neag, O. Cadar, *Nanomaterials* 10 (2020) 580.
- [59] R. Bhargava, P.K. Sharma, R.K. Dutta, S. Kumar, A.C. Pandey, N. Kumar, *Mater. Chem. Phys.* 120 (2010) 393–398.
- [60] M. Zahir, M.M. Rahman, K. Irshad, M.M. Rahman, *Nanomaterials* 9 (2019) 1773.
- [61] S. Sun, X. Zhang, Y. Sun, S. Yang, X. Song, Z. Yang, *Phys. Chem. Chem. Phys.* 15 (2013) 10904–10913.
- [62] A.M. Ismail, A.A. Menazea, H.A. Kabary, A.E. El-Sherbiny, A. Samy, *J. Mol. Struct.* 1196 (2019) 332–337.
- [63] M. Sajjad, I. Ullah, M.I. Khan, J. Khan, M.Y. Khan, M.T. Qureshi, *Results Phys.* 9 (2018) 1301–1309.
- [64] S.S. Chawhan, D.P. Barai, B.A. Bhanvase, *Therm. Sci. Eng. Prog.* 25 (2021), 100928.
- [65] V. Kusigerski, E. Illes, J. Blanus, S. Gyergyek, M. Boskovic, M. Perovic, V. Spasojevic, *J. Magn. Magn. Mater.* 475 (2019) 470–478.
- [66] C.W. Wong, Y.S. Chan, J. Jeevanandam, K. Pal, M. Bechelany, M. Abd Elkoudous, G.S. El-Sayyad, *J. Clust. Sci.* 31 (2020) 367–389.
- [67] J. Jeevanandam, Y.S. Chan, M.K. Danquah, *ChemistrySelect* 2 (2017) 10393–10404.
- [68] T. Tangcharoen, C. Kongmark, *J. Adv. Ceram.* 8 (2019) 352–366.
- [69] S. Chitra, P. Bargavi, M. Balasubramaniam, R.R. Chandran, S. Balakumar, *Mater. Sci. Eng. C* 109 (2020), 110598.
- [70] S. Meghana, P. Kabra, S. Chakraborty, N. Padmavathy, *RSC Adv.* 5 (2015) 12293–12299.
- [71] P.C. Dey, R. Das, *Indian J. Phys.* 92 (2018) 1099–1108.
- [72] W. Xie, J. Wang, L. Fu, Q. Tan, X. Tan, H. Yang, *Appl. Clay Sci.* 185 (2020), 105374.
- [73] S. Tomar, S. Gupta, S. Mukherjee, A. Singh, S. Kumar, R.K. Choubey, *Semiconductors* 54 (2020) 1450–1458.
- [74] S. Mustapha, M.M. Ndamitso, A.S. Abdulkareem, J.O. Tijani, D.T. Shuaib, A. K. Mohammed, A. Sumaila, *Adv. Nat. Sci. Nanosci. Nanotechnol.* 10 (2019), 045013.
- [75] N. Rani, S. Chahal, A.S. Chauhan, P. Kumar, R. Shukla, S.K. Singh, *Mater. Today: Proc.* 12 (2019) 543–548.
- [76] O.S. Oluwafemi, B.M.M. May, S. Parani, N. Tsolekile, *Mater. Sci. Eng. C* 106 (2020), 110181.
- [77] L. Martinaga Pintarić, M. Somogi Škoc, V. Ljoljić Bilić, I. Pokrovac, I. Kosalec, I. Rezić, *Polymers* 12 (2020) 1210.
- [78] Z. Remes, H. Kozak, B. Rezek, E. Ukraintsev, O. Babchenko, A. Kromka, H. A. Girard, J.C. Arnault, P. Bergonzo, *Appl. Surf. Sci.* 270 (2013) 411–417.
- [79] S. Yousefi, B. Ghasemi, M. Tajalli, A. Asghari, *J. Alloys Compd.* 711 (2017) 521–529.
- [80] D. An, X. Ding, Z. Wang, Y. Liu, *Colloids Surf. A Physicochem. Eng. Asp.* 356 (2010) 28–31.
- [81] P. Tamilselvi, A. Yelilarasi, M. Hema, R. Anbarasan, *Nano Bulletin* 2 (2013), 130106.
- [82] G. Balakrishnan, R. Velavan, K.M. Batoo, E.H. Raslan, *Results Phys.* 16 (2020), 103013.
- [83] M. Shaheen, I.A. Bhatti, A. Ashar, M. Mohsin, J. Nisar, M.M. Almonief, M. Iqbal, *Z. Phys. Chem* 235 (2021) 1395–1412.
- [84] S. Muthukumar, R. Gopalakrishnan, *Opt. Mater.* 34 (2012) 1946–1953.
- [85] M. Ikram, T. Inayat, A. Haider, A. Ul-Hamid, J. Haider, W. Nabgan, A. Saeed, A. Shahbaz, S. Hayat, K. Ul-Ain, *Nanoscale Res. Lett.* 16 (2021) 1–11.
- [86] M. Manzoor, A. Rafiq, M. Ikram, M. Nafees, S. Ali, *Int. Nano Lett.* 8 (2018) 1–8.
- [87] C. Belkhaoui, N. Mzabi, H. Smaoui, P. Daniel, *Results Phys.* 12 (2019) 1686–1696.
- [88] D. Thamilvanan, J. Jeevanandam, Y.S. Hii, Y.S. Chan, *Can. J. Chem. Eng.* 99 (2021) 502–518.
- [89] P.J. Anderson, P.L. Morgan, *Trans. Faraday Soc.* 60 (1964) 930–937.
- [90] J. Amodeo, S. Merkel, C. Tromas, P. Carrez, S. Korte-Kerzel, P. Cordier, J. Chevalier, *Crystals* 8 (2018) 240.
- [91] K. Omri, S. Goudria, *J. Mater. Sci. Mater. Electron.* 32 (2021) 17021–17031.
- [92] A. Vanaja, M. Suresh, J. Jeevanandam, *Int. J. Nanosci. Nanotechnol.* 15 (2019) 277–286.
- [93] K.S. Ahmad, S.B. Jaffri, *Open Chem.* 16 (2018) 556–570.
- [94] A.R. Oganov, M.J. Gillan, G.D. Price, *J. Chem. Phys.* 118 (2003) 10174–10182.
- [95] M. Aslam, G. Gopakumar, T.L. Shoba, I.S. Mulla, K. Vijayamohan, S. K. Kulkarni, J. Urban, W. Vogel, *J. Colloid Interface Sci.* 255 (2002) 79–90.
- [96] V. Shanmugam, K.S. Jeyaperumal, *Appl. Surf. Sci.* 449 (2018) 617–630.
- [97] P. Nyamukamba, O. Okoh, H. Heroe, R. Taziwa, S. Zinya, *Synthetic methods for titanium dioxide nanoparticles: a review*, Chap. 8, Yang, D. (Ed.), (2018), *Titanium Dioxide - Material for a Sustainable Environment*. InTech. doi: <https://doi.org/10.5772/intechopen.70290>.
- [98] X. Guo, Q. Zhang, X. Ding, Q. Shen, C. Wu, L. Zhang, H. Yang, *J. Sol-Gel Sci. Technol.* 79 (2016) 328–358.
- [99] N. Sakai, T. Nakano, K. Yanaba, S. Imazeki, *J. Sol-Gel Sci. Technol.* 88 (2018) 379–385.
- [100] R.K. Singh, S. Kannan, *Mater. Sci. Eng. C* 45 (2014) 530–538.
- [101] A.T. Brant, D.A. Buchanan, J.W. McClory, P.A. Dowben, V.T. Adamiv, Y.V. Burak, L.E. Halliburton, *J. Lumin.* 139 (2013) 125–131.
- [102] H. Gupta, L.-S. Fan, *Ind. Eng. Chem. Res.* 41 (2002) 4035–4042.
- [103] C.-H. Lin, J.-H. Chao, C.-H. Liu, J.-C. Chang, F.-C. Wang, *Langmuir* 24 (2008) 9907–9915.
- [104] M.P. Nikolova, M.S. Chavali, *Biomimetics* 5 (2020) 27.
- [105] J.R. Morones, J.L. Elechiguerra, A. Camacho, K. Holt, J.B. Kouri, J.T. Ramirez, M. J. Yacamán, *Nanotechnology* 16 (2005) 2346.
- [106] H. Lee, R.G. Larson, *Molecules* 14 (2009) 423–438.
- [107] F. Avila-Salas, R.I. González, P.L. Ríos, I. Araya-Durán, M.B. Camarero, *J. Chem. Inf. Model.* 60 (2020) 2966–2976.
- [108] Y. Shan, T. Luo, C. Peng, R. Sheng, A. Cao, X. Cao, M. Shen, R. Guo, H. Tomás, X. Shi, *Biomaterials* 33 (2012) 3025–3035.
- [109] Z. Xiong, C.S. Alves, J. Wang, A. Li, J. Liu, M. Shen, J. Rodrigues, H. Tomás, X. Shi, *Acta Biomater.* 99 (2019) 320–329.
- [110] Y. Zhang, X. Liu, L. Li, Z. Guo, Z. Xue, X. Lu, *Anal. Methods* 8 (2016) 2218–2225.
- [111] M. Mecozzi, M. Pietroletti, M. Scarpiniti, R. Acquistucci, M.E. Conti, *Environ. Monit. Assess.* 184 (2012) 6025–6036.
- [112] Y. Lin, J. Ren, X. Qu, *Acc. Chem. Res.* 47 (2014) 1097–1105.
- [113] L. Lo Leggio, T.J. Simmons, J.-C.N. Poulsen, K.E.H. Frandsen, G.R. Hemsworth, M. A. Stringer, P. Von Freiesleben, M. Tovborg, K.S. Johansen, L. De Maria, *Nat. Commun.* 6 (2015) 1–9.
- [114] S. Dakhmouche Djekrif, L. Bennamoun, F.Z.K. Labbani, A. Ait Kaki, T. Nouadri, A. Paus, Z. Meraihi, L. Gillmann, *Catalysts* 11 (2021) 1438.
- [115] Z. Han, H. Shaofeng, L. Zhang, F. Yunchang, G. Fengzhe, W. Dongyue, Z. Meijin, *Indian J. Biochem. Biophys.* 57 (2020) 411–431.
- [116] T.H. Nguyen, S.-L. Wang, A.D. Nguyen, M.D. Doan, T.N. Tran, C.T. Doan, V. B. Nguyen, *Mar. Drugs* 20 (2022) 283.
- [117] B.F. Shaw, G.F. Schneider, B. Bilgicer, G.K. Kaufman, J.M. Neveu, W.S. Lane, J. P. Whitelegge, G.M. Whitesides, *Protein Sci.* 17 (2008) 1446–1455.
- [118] A. Asthana, A.S. Chauhan, P.V. Diwan, N.K. Jain, *AAPS PharmSciTech* 6 (2005) E536–E542.
- [119] S. El Kazzouli, S. Mignani, M. Bousmina, J.-P. Majoral, *New J. Chem.* 36 (2012) 227–240.
- [120] M.A. Kainat, F. Khan, S. Ali, M. Faisal, Z. Rizwan, N. Hussain, Z. Zaman, M. N. Afsheen, N. Uddin, Bibi, Saudi, *J. Biol. Sci.* 28 (2021) 5157–5167.

- [121] M.A. Ammulu, K. Vinay Viswanath, A.K. Giduturi, P.K. Vemuri, U. Mangamuri, S. Poda, J. Genet. Eng. Biotechnol. 19 (2021) 21.
- [122] A.A.-A. Ahlam, N.A.E.-R. Soheir, Food Nutr. Sci. 12 (2021) 308.
- [123] J.N. D'Souza, G.K. Nagaraja, K. Meghana Navada, S. Kouser, D.J. Manasa, Ceram. Int. 47 (2021) 29620–29630.



Aptamer-navigated copolymeric drug carrier system for *in vitro* delivery of MgO nanoparticles as insulin resistance reversal drug candidate in Type 2 diabetes

Kei X. Tan^{a,1}, Jaison Jeevanandam^a, Sharadwata Pan^b, Lau Sie Yon^a, Michael K. Danquah^{c,*}

^a Department of Chemical Engineering, Curtin University, Sarawak, 98009, Malaysia

^b School of Life Sciences Weihenstephan, Technical University of Munich, 85354, Freising, Germany

^c Department of Chemical Engineering, University of Tennessee, Chattanooga, TN, 37403, United States

ARTICLE INFO

Keywords:

Aptamer
MgO nanoparticles
Biopolymer
Targeted drug delivery
Microparticles
Encapsulation
Type 2 diabetes

ABSTRACT

Magnesium Oxide (MgO) nanoparticles are known to play a significant role in lowering the production of lipids and serum glucose for diabetes treatment. Additionally, the emergence of aptamers has created new opportunities in the realization of smart drug delivery systems, mainly attributing to their abilities to be altered at the molecular level, and subsequently be conjugated onto biopolymers harbouring specific drugs, in order to navigate specific cellular sites. The current work reports the synthesis of a multifunctional aptamer-navigated particulate delivery system (DPAP), harbouring MgO (synthesized via chemical - MgO₁ and green - MgO₂ approaches) nanoparticles, to target 3T3-L1 diabetic cells. *In vitro* performance indicators, including encapsulation efficiency, targeting capability, cellular transfection efficiency, and insulin reversal capacity, were investigated. While the DLS analysis indicated hydrodynamic sizes of 766.6 nm and 641.3 nm for the DPAP-MgO₁ and DPAP-MgO₂ formulations, respectively; and zeta potentials of +5.28 mV and -0.025 mV, for the same formulations, respectively. Additionally, DPAP-MgO₂ offered better encapsulation efficiency and loading capacity of 93.69% and 0.03 mg MgO/mg PLGA, respectively. 3,5-Dinitrosalicylic acid (DNS) assessment showed that both DPAP-MgO₁ and DPAP-MgO₂ particulate systems enhanced the *in vitro* cellular uptake, as well as the insulin resistance reversal ability of the 3T3-L1 cells. The outcomes from the current work demonstrate the potential of DPAP particulate system as an effective and promising carrier, for the delivery of MgO nanoparticles in diabetes treatment.

1. Introduction

Conventional approaches to disease targeting and treatment often result in poor therapeutic outcomes and undesirable side effects, due to the non-specific nature of active drug molecules [1,2]. Over the past decades, research has focused on improving the current drug delivery systems for enhanced targeting and controlled release characteristics. The synthesis of affinity ligands, such as aptamers, which bind onto specific cell targets, has created new opportunities to navigate drug molecules and deliver them to desired sites. Aptamers, mostly generated by SELEX (Systematic Evolution of Ligands by Exponential Enrichment), are single-stranded oligonucleotides made up of either DNA or RNA. They interact and bind to their cognate target molecules with a high affinity, by adopting unique 3D conformational structures to boost

interactions [3,4]. As discussed previously in our earlier publications [5], the unique characteristics of aptamers, including high sensitivity and specificity, chemical and thermal stability, and bioavailability, make them a promising affinity ligand for improved *in vivo* cell targeting and drug delivery. However, practical applications of the aptamer-mediated cell targeting strategies face biophysical and biochemical challenges, due to the small size of the aptamers, serum degradation, rapid systemic clearance, and the aptamer-cell membrane barrier [6,7]. Subsequently, aptamers may possess a short circulation half-life during the cellular events.

In order to overcome these limitations and fully exploit the potential of aptamer-mediated targeting approaches, biodegradable polymeric carrier systems can be used to harbour and protect the ligand and drug molecules during cellular trafficking. There are diverse drug-loaded

* Corresponding author.

E-mail addresses: tan.kei.xian@postgrad.curtin.edu.my (K.X. Tan), jaison.jeevanandam@postgrad.curtin.edu.my (J. Jeevanandam), sharadwata.pan@tum.de (S. Pan), johnlsy@curtin.edu.my (L.S. Yon), michael-danquah@utc.edu (M.K. Danquah).

¹ Current Address: School of Materials Science and Engineering, Nanyang Technological University, 639798, Singapore.

<https://doi.org/10.1016/j.jddst.2020.101764>

Received 9 February 2020; Received in revised form 19 April 2020; Accepted 19 April 2020

Available online 22 April 2020

1773-2247/ © 2020 Elsevier B.V. All rights reserved.

aptamer-polymeric bioconjugates, formulated against different targets. These include the anti-PDGF aptamer conjugated-E10030 drug encapsulated PEG formulation, to treat neovascular age-related muscular degeneration [6]; the nucleolin-targeting AS1411 polymeric system, to treat myeloid leukemia, glioma, and breast cancer [8–10]; the EpCAM-conjugated PEI nanoparticles, to treat breast and retinoblastoma tumours [11]; and the A10 RNA aptamer-linked PLGA-PEG particles, to target prostate cancer cells [12,13]. The challenge of developing an efficient aptamer/drug carrier lies in the design of a biopolymeric system, which is capable of eliminating the particles-cell barrier and improving circulation half-life, as well as enhancing the drug uptake rate by the target cells over a sustained period of time in a controlled release fashion, in order to obtain effective clinical responses at specific sites.

Magnesium is a vital and one of the most prevalent cations occurring naturally in more than 300 human enzymes. It plays important roles in many physiological reactions, including glucose and lipid metabolism [14–16]. Magnesium is widely used in complementary therapies for diabetes treatment [17], due to its modulatory effects on glucose oxidation and transport, and insulin secretion [18]. Magnesium oxide (or MgO) nanoparticles are biodegradable and non-toxic, with numerous studies reporting on their efficacy for treating diabetes. For instance, Naghsh and Kazemi [19] demonstrated the effects of nano-magnesium oxide in reducing the serum glucose level and various lipid types, in diabetes induced mice. Another study reported that magnesium oxide nanoparticles are capable of significantly altering the convulsion onset and death time in diabetic mice, with a higher anticonvulsive effect compared to the conventional magnesium oxide forms [20]. A recent study indicated the capability of magnesium oxide nanoparticles in triggering anti-oxidative, anti-diabetic and anti-apoptotic functions in the pancreatic islet [21]. Aside being a potential therapeutic agent for treating diabetes, magnesium oxide nanoparticles are also effective in addressing other medical disorders, such as anxiety and hypertension [22–24]. Recently, we have proved that MgO nanoparticles have potential in reversing insulin resistance in diabetic cells [25].

In this work, an aptamer-navigated polymeric system (DPAP) is used as a delivery carrier to deliver encapsulated magnesium oxide nanoparticles to diabetic 3T3L1 cell lines, in the presence of target molecules. DPAP was selected as a potential formulation system for the antidiabetic nanoparticles, as they are proven to be less toxic compared to the conventional PLGA and PEI polymers, as shown in our previous studies [26]. The effectiveness of the DPAP formulation as a targeted delivery vehicle, in terms of targeting capability and transfection efficiency, is evaluated. The multifunctional DPAP formulation is synthesized using PLGA and PEI copolymeric system, including a thrombin-specific DNA aptamer. The DPAP particulate delivery system constitutes a layer-by-layer organization, with the drug, i.e., MgO nanoparticles, as the payload [D], encapsulated within the inner polymeric core made of PLGA, i.e., [P]. Thrombin-specific DNA aptamer molecules are conjugated onto the surface of the PLGA layer as the targeting elements, i.e., [A]; and finally, the PEI polymeric particles are intercalated with the aptamer as the outermost layer [P]. We have previously reported on the biophysical characteristics of DPAP formulation and demonstrated its controlled drug release characteristics under *in vitro* conditions [27,28]. However, there is no previous reports on MgO nanoparticle formulation for reversing insulin resistance in diabetic cells. Thus, the present work evaluates the efficacy of the DPAP particulate system to effectively deliver MgO nanoparticles to the target 3T3-L1 cells, as an insulin resistance reversal drug candidate in diabetes treatment.

2. Materials and methods

2.1. Materials

Branched PEI of 25 kDa molecular weight; PLGA (50:50) with molecular weight of 30–60 kDa; N-hydroxysuccinimide (NHS) ($\geq 98\%$ (HPLC)) with 115.09 g/mol molecular weight; 1-ethyl-3-(3-dimethylaminopropyl)-carbodiimide (EDC) with 191.70 g/mol molecular weight (powdered form, premium quality level, commercial grade); Acetone (laboratory reagent grade, $\geq 99.5\%$) with molecular weight of 58.08 g/mol; Poly(vinyl alcohol) (PVA) with molecular weight of 31–50 kDa (powdered form, 98–99% hydrolysed); and Phosphate buffered saline (PBS) (water-based salt buffer solution; 1 tablet dissolved in 200 ml deionised water has pH 7.4, 0.137 M sodium chloride, 0.01 M phosphate buffer, 0.0027 M potassium chloride at 25 °C) was purchased from Sigma Aldrich (Malaysia). Thrombin-targeting DNA aptamer (15-mer) with sequence 5'-GGT TGG TGT GGT TGG-3' (PCR grade, 225 OD, 5.0 μ mole scale) was obtained from 1st BASE (Malaysia). Magnesium precursors, which are magnesium nitrate hexahydrate (98%), were purchased from Alfa Aesar (USA) and fresh leaves of *Amaranthus tricolor* (red spinach) were obtained from the local market in Sarawak (Malaysia) for green synthesis of hexagonal shaped MgO nanoparticles. Similarly, magnesium acetate tetra hydrate (98% purity), as magnesium precursor, was procured from Alfa Aesar (USA) and citric acid (99.9% purity), as gelling agent, was obtained from Fisher scientific (Singapore). Ethanol (99.4% purity) as solvent was obtained from Fisher scientific (Singapore) for the chemical synthesis of hexagonal shaped MgO nanoparticles. All the reagents and chemicals were used directly without any further purification. 3T3-L1 adipose cell line was obtained from the National Cell Culture Society (NCCS), Pune, India. 3T3-L1 is a common pre-adipose cell line obtained from murine Swiss 3T3 cells and is widely used to study obesity-associated characteristics and glucose utilization [29–31].

2.2. Synthesis of MgO nanoparticles

Two main approaches, i.e., chemical and green biosynthesis strategies, were employed to synthesize the MgO nanoparticles. MgO nanoparticles were synthesized by a chemical approach using the sol-gel method as described by Jeevanandam et al. [32]. An equimolar ratio of magnesium precursor and the gelling agent were dissolved in ethanol separately and then mixed to form a gel of the magnesium network at pH 5. The gel was then subjected to aging for 12 h and drying for 24 h at 100 °C to form a sol-gel powder. The obtained sol-gel powders were calcined in a box furnace (Carbolite 1200 °C heavy duty box furnace) at 650 °C for 2 h at a heating rate of 5 °C/min to form pure, hexagonal shaped MgO nanoparticles. Green synthesized MgO nanoparticles were generated using *A. tricolor* plant leaf extracts, as described previously by Jeevanandam et al. [33]. Briefly, the fresh leaves were extracted using distilled water in a w/v ratio of 1:10. The mixtures were shaken for 20 min at 350 RPM and heated at 100 °C before filtration. The magnesium precursors were then mixed with the aqueous leaf extracts with constant stirring and heating at 60 °C for 10 min. MgO₁ is used to designate the chemically synthesized MgO nanoparticles; whilst MgO₂ is used for the same generated via green synthesis. Both types were used to investigate and compare their effects on biophysical properties, encapsulation efficiency, cellular uptake, and cytotoxicity of DPAP-MgO formulations. Dynamic Light Scattering (DLS) was carried out using a Zetasizer Nano ZS (Malvern, Model ZEN3600, UK) to determine the average D [4,3] hydrodynamic size, particle size distribution, and zeta potential of different MgO

nanoparticles and DPAP carrying MgO nanoparticles. The morphologies of the formulations were characterized using Transmission Electron Micrograph (TEM).

2.3. *In vitro* generation of DPAP formulation carrying MgO drug nanoparticles

The DPAP formulation was generated using a double emulsion water-in-oil-in-water (w/o/w) method integrated with ultra-sonication as reported previously by our group Tan, Danquah [27]. MgO nanoparticles were encapsulated within the inner core of DPAP micro-par-

$$\text{Encapsulation efficiency (\%)} = \frac{\text{Amount of loaded MgO1 or MgO2 or aptamer}}{\text{Total amount of initially added MgO1 or MgO2 or aptamer applied}} \times 100$$

ticles as drug molecules. Two DPAP-MgO micro-particulate systems were generated: 1) DPAP formulation encapsulating chemically synthesized MgO nanoparticles (DPAP-MgO₁); and 2) DPAP formulation carrying green synthesized MgO nanoparticles (DPAP-MgO₂). Basically, 0.001 M each of MgO₁ and MgO₂ nanoparticles, were sonicated for 15 min before encapsulation into PLGA polymeric particles. 10 w/v% PLGA was prepared by dissolving PLGA into acetone to produce a polymeric matrix. Each MgO nanoparticle solution was added to the PLGA polymeric matrix and sonicated for 2 min at 70% amplitude, and 0.7 s pulse cycle using Labsonic[®] M ultra-sonicator. 2% w/v PVA emulsifying agent was added to the mixture to solidify the DP (MgO-P) emulsion droplets under constant ultrasonication. Next, the DP mixture was shaken gently at 200 RPM for 2 h at ambient temperature to evaporate the organic solvent from the emulsion. The DP mixture was further centrifuged at 4 °C and 4000 RPM for 20 min using a Universal 320R centrifuge to remove the residual organic solvent and PVA, followed by freeze-drying for 48 h to generate solid MgO-entrapped PLGA (DP) particles.

2.4. Aptamer conjugation via EDC and NHS coupling chemistry

The coupling of thrombin-specific DNA aptamer molecules onto DP particles was achieved via EDC and NHS activation chemistry. EDC was used to activate the carboxyl functional groups of DP, whilst NHS was activated to substitute EDC with hydroxyl functional groups. Further, amine-terminated aptamer molecules were conjugated onto the surface of DP particles. This was achieved via the formation of covalent amide bond between the amino group at the 3' end of the aptamer molecules, and DP carboxylic groups via enhanced electrophilicity. Initially, DP formulation was incubated with 100 mM NHS and 400 mM EDC in PBS buffer at 200 RPM for 1 h prior to 20-min centrifugation at 4 °C and 4000 RPM. Next, 100 μM aptamer was incubated with the generated NHS-activated DP-COOH at 200 RPM for 1 h followed by centrifugation at 4 °C and 4000 RPM for 5 min to form aptamer-coupled DP (DPA) particles. The DPA particulates were added to 12% w/v PEI polymeric stock to produce both MgO₁- and MgO₂-loaded PLGA-Aptamer-PEI (DPAP-MgO₁ and DPAP-MgO₂) formulations.

2.5. Encapsulation efficiency and loading capacity of DPAP formulation

The concentration of encapsulated MgO₁ and MgO₂ drug nanoparticles was measured using UV-visible spectrophotometry (PerkinElmer, Lambda 25 UV/Vis Double Beam) at 320–330 nm for MgO₁, and 320 nm for MgO₂ nanoparticles, respectively. A slight difference in the measuring wavelength between MgO₁ and MgO₂ is due to the variations in the synthesis approaches, where different functional groups (carboxyl group in MgO₁ and phytochemicals in MgO₂) played a significant role in nanoparticle formation that eventually alters their size and optical absorbance. The concentration of encapsulated MgO

nanoparticles within the DPAP formulation was calculated as the difference between the initial concentration of MgO and the amount of free MgO molecules in the supernatant, after the formation of DP. The concentrations of free MgO₁ and MgO₂ nanoparticles were determined after centrifuging DP at 4000 RPM and 4 °C for 20 min, and analysing the supernatant. The loading capacities and encapsulation efficiencies of DPAP-MgO₁ and DPAP-MgO₂ formulations were estimated using the following equations:

$$\text{Loading capacity} = \frac{\text{Amount of entrapped MgO1/MgO2 (mg)}}{\text{Original amount of PLGA added (mg)}}$$

2.6. *In vitro* characterization of DPAP-MgO particulate system

The zeta potential, D[4,3] hydrodynamic size, and size distribution (polydispersity index or PDI) of DPAP-MgO co-polymeric complex carrying MgO nanoparticles were analysed using the Zetasizer Nano ZS based on the dynamic light scattering (DLS) measurement. The Malvern DTS software was utilized for data collection and subsequent analysis.

2.7. 3,5-Dinitrosalicylic acid (DNS) assay

DNS assay was carried out by incubating DPAP-MgO₁ and DPAP-MgO₂ samples with 3T3 L1 cells over a 25-h incubation duration. 3T3 L1 cells were kept in the DMEM-thrombin medium with penicillin (100 U/ml), 10% FBS, and streptomycin (100 μg/ml), in a humidified environment of 50 μg/ml carbon dioxide at 37 °C. 5 mL of the pretreated 3T3 L1 cell was added to a 6-well plate before the addition of 1 mL DPAP-MgO₁ and DPAP-MgO₂ samples at different dosages. Optical densities and concentrations were determined at various time intervals. The DMEM medium with glucose was tested with DNS assay after every 5 h to determine the insulin resistance reversal ability of DPAP-MgO₁ and DPAP-MgO₂ formulations. The color intensities of the tested samples were also monitored.

2.8. Statistical analysis

All experiments were conducted in triplicate and the mean magnitudes along with standard deviations are reported as final results.

3. Results and discussion

3.1. DPAP formulation carrying MgO nanoparticles and degradation mechanism

DPAP targeted delivery system was developed *in vitro* via w/o/w double emulsion technique in conjunction with ultra-sonication. Fig. 1 illustrates the schematics of the DPAP formulation, encapsulated with MgO nanoparticles as the drug payloads within the inner hydrophobic PLGA core. The thrombin-targeting DNA aptamer molecules, acting as the targeting elements, were coupled via EDC/NHS chemistry onto the outer surface of the PLGA particles. The aptamer molecules are vital in navigating the DPAP system towards target cells, through specific surface protein recognition. This reduces the non-specific interactions between DPAP and non-targeted cells. Hence, a sufficient concentration of the functional drug molecules may be delivered to the target sites to trigger an optimal remedial response. The outer layer of the DPAP is created from molecular intercalation between the aptamer molecules, and the positively charged, hydrophilic PEI particles.

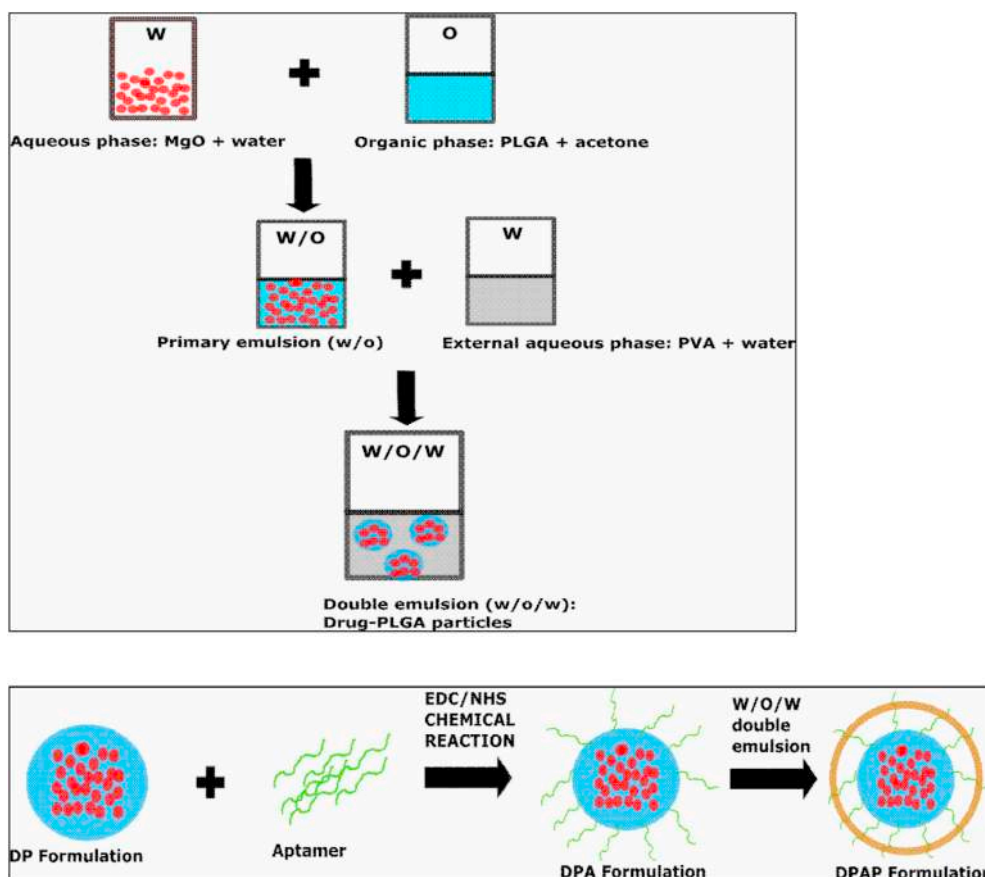


Fig. 1. Schematics of the DPAP formulation process encapsulating MgO nanodrug particles and aptamer navigating molecules.

The DPAP design concept is based on improving cell-targeting, using aptamers as the targeting ligand, in order to deliver drug molecules to the desired sites. The slightly electropositive characteristic of DPAP reduces cellular barriers and electrostatic repulsion that could hinder effective DPAP-cell membrane interactions. The multi-layer design of DPAP using a co-polymer assembly, is deliberated to give extra protection to its bioactive components, such as the drug molecules and the targeting elements. The co-polymeric assembly provides shielding from challenging physiological environments, including initial drug burst, short circulating half-lives, endonuclease-mediated degradation, and non-specific systemic clearance. Also, the co-polymeric feature facilitates a pH-dependent degradation mechanism, allowing the control of DPAP degradation under the right intracellular event (such as the endosome) to release encapsulated drug molecules. The effective transfection efficiency and proton sponge effect of PEI particles offer high internalization and endosomal escape of entrapped drug molecules towards the nucleus to enhance therapeutic outcomes. The hydrolytic degradation of polymeric particles can offer a controlled

and sustained drug release over a desired time period. Hence, the DPAP design concepts have the potential to address some of the limitations associated with the conventional drug delivery system.

3.2. Zeta potential and hydrodynamic size analysis of DPAP-MgO formulations

The average D [4,3] hydrodynamic particle size, zeta potential and polydispersity index (PdI) of DPAP, DPAP-MgO₁, and DPAP-MgO₂ are presented in Table 1 and Fig. 2. This study investigated the biophysical characteristics of the DPAP particulate systems post MgO nanoparticle encapsulation. The average D [4,3] hydrodynamic size of DPAP micro-particles were 615.6 nm, compared to the average size of 766.6 nm (DPAP-MgO₁) and 641.3 nm (DPAP-MgO₂). The minor increase in the hydrodynamic size indicates a successful incorporation of the MgO nanoparticles into the DPAP architecture. Even though, the size of the DPAP is above 500 nm, it is highly beneficial as nanocarrier due to their double protective emulsion design for MgO nanoparticles, avoid their

Table 1

The average D[4,3] hydrodynamic size, PdI and zeta potential of DPAP-MgO₁, DPAP-MgO₂, and DPAP formulation, as well as MgO₁ and MgO₂ nanoparticles at pH 7.

Formulation	Z-average (d.nm)	PdI	Zeta potential (mV)
MgO ₁ -PLGA-Apt-PEI	766.6 ± 182.12	0.572 ± 0.051	+5.28 ± 0.499
MgO ₂ -PLGA-Apt-PEI	641.3 ± 72.14	0.624 ± 0.027	-0.0245 ± 0.010
DPAP	615.6 ± 23.99	0.665 ± 0.063	+9.07 ± 0.453

Drug sample	Generation Method	Shape	Z-average (d.nm)	PdI	Zeta potential (mV)
MgO ₁	Chemically synthesized	Hexagon	43.8 ± 0.519	0.615 ± 0.018	-7.21 ± 0.211
MgO ₂	Green synthesized	Hexagon	43.82 ± 0.361	0.454 ± 0.023	-3.39 ± 0.784

[30,31].

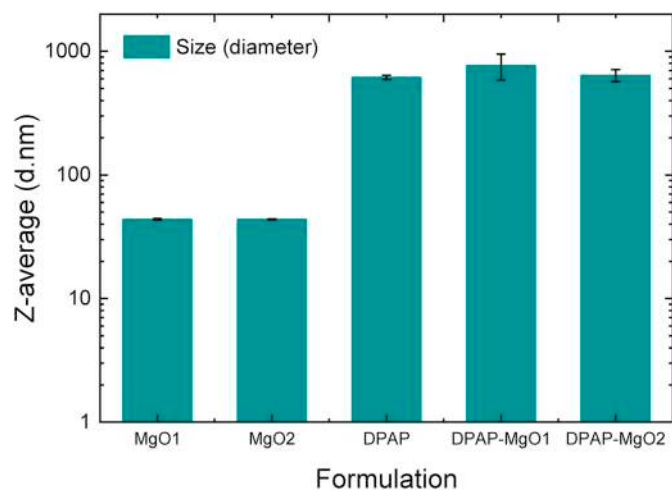


Fig. 2. DLS data showing the average D [4,3] hydrodynamic size of DPAP carrying MgO₁/MgO₂ nanoparticles, in comparison to that of the original MgO₁/MgO₂ nanoparticles, and DPAP formulation without any drug molecule.

disintegration into ions in biological barriers and fluids, and deliver them at a target site (diabetic cells) in a controlled fashion [34]. The average hydrodynamic size of MgO₁ and MgO₂ nanoparticles was ~43.8 nm (see Table 1), with a hexagonal shape, as shown in Fig. 3. Hexagonal MgO nanoparticles have been reported to provide enhanced physiological features due to their edge effects [33,35]. DPAP-MgO₁ showed a slightly larger average D [4,3] hydrodynamic diameter than DPAP-MgO₂, and this may be due to the presence of residual plant-based biochemical or biomolecules, which also interact with PLGA to increase the strength of electrostatic interactions, resulting in a smaller average diameter. Further, the agglomeration in MgO₁ (Fig. 3 (a)) due to synthetic functional groups play a key role in increasing their average D, compared to MgO₂, which eventually affects their encapsulation efficiency and loading capacity. DPAP-MgO formulations in the micron size range, are effective in enhancing the resident time of encapsulated drug molecules at localized desired sites, via micro-particulate adherence and aggregation mechanisms [36]. In addition, DPAP-MgO micro-particles possess the ideal size for respiratory or nasal administrative route and intranasal immunization [37–39]. The average hydrodynamic diameter of both DPAP-MgO₁ and DPAP-MgO₂, being smaller than 2 μ m, promotes an effective surface area for endocytosis and phagocytosis. As a result, the delivery of the drug is enhanced by the increased amount of internalized drug molecules into the desired cells [40]. A number of reported micro-particulate delivery

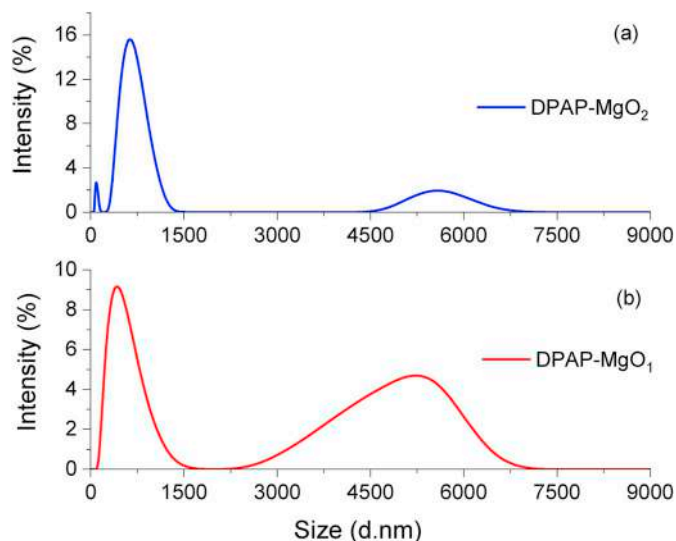


Fig. 4. Particle size distribution data for (a) DPAP-MgO₁ and (b) DPAP-MgO₂ formulations.

systems have demonstrated their efficacies in shielding payloads from challenges, such as short circulating half-life, enzymatic attacks, low cellular permeability, and systemic clearance [41,42].

Fig. 4(a) shows the particle size distribution of the DPAP-MgO₁ micro-particles with 766.6 nm average D[4,3] hydrodynamic size. Peak 1 (from left) has a diameter of 469.5 nm, with 84.4% intensity and 234.0 nm standard deviation; and peak 2 has a diameter of 5560 nm, with 15.6% intensity and 805.3 nm standard deviation. Fig. 4(b) shows 3 different peaks for the DPAP-MgO₂ formulation. Peak 1 (from left) has a diameter of 94.18 nm, with 11.3% intensity and 20.33 nm standard deviation; peak 2 has a diameter of 646.6 nm, with 85.7% intensity and 183.6 nm standard deviation; peak 3 has a diameter of 5560 nm, with 2.9% intensity. The highest peak of DPAP-MgO₁ (peak 1) and the same corresponding to DPAP-MgO₂ (peak 2) show intensities that constitute the characteristics of the individual particles. The presence of peak 2 in DPAP-MgO₁ size distribution, is due to particulate aggregation formed via inter-particle collisions amongst DPAP micro-particles, during the solvent evaporation step of the synthesis process. The peak 1 in the size distribution of DPAP-MgO₂ formulation, could be due to electro-kinetic leaching of plant-based biomolecules accompanying the green synthesized MgO nanoparticles, whilst peak 3 could be a consequence of aggregation, as explained earlier. Even though, the average particle size of

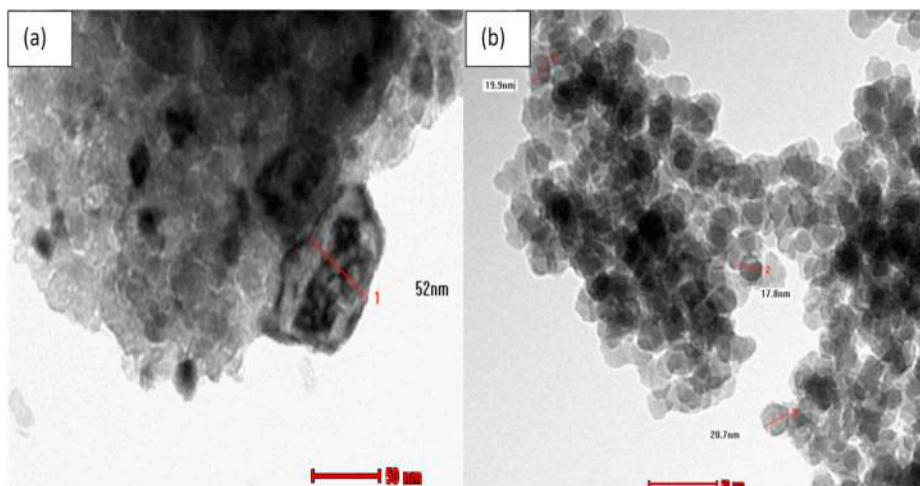


Fig. 3. TEM Analysis of (a) MgO₁ and (b) MgO₂ nanoparticles with a hexagonal shape.

the system seems to be larger than the definition of a nanoparticles (≤ 100 nm), it is within the acknowledged range for a nanoparticle of a biological origin or nanoencapsulation (≤ 1000 nm) [43]. Further, the MgO nanoparticles are ~ 50 nm in size, which is encapsulated by double emulsion layer to form the DPAP system, and eventually increases their average particle size. This double layer encapsulation of nanoparticles is required for oral drug delivery, to protect them from digestive system and effectively delivery in the target site [44]. Each layer will disintegrate or dissolve in each stage of digestion and reduces in size, which finally leads to the delivery of ~ 50 nm sized MgO nanoparticles towards the adipose cells. Thus, it is evident that larger size of nanoformulation is beneficial for the effective delivery of nanoparticles. Polydispersity Index, i.e., PDI, is a measure of the degree of uniformity of particulate size distribution. The size distributions in Fig. 4(a) and (b) present PDI values of 0.399 for DPAP-MgO₁, and 0.531 for DPAP-MgO₂, showing that the particle size distributions are moderately polydispersed.

The zeta potentials of DPAP-MgO₁, DPAP-MgO₂ and DPAP particulate systems, as well as the original MgO₁ and MgO₂ nanoparticles are listed in Table 1. Both MgO₁ and MgO₂ nanoparticles were electronegative with a surface charge of -7.21 mV and -3.39 mV respectively. This is due to the anionic oxide deposits on the surface of MgO nanoparticles. The zeta potential of PLGA is more electropositive, facilitating electrostatic interactions with the negatively charged MgO nanoparticles and enhanced encapsulation within the core of DPAP. The zeta potential of the DPAP formulation without MgO nanoparticles was $+9.07$ mV. After the introduction of MgO nanoparticles into the DPAP architecture, the resulting DPAP-MgO system became marginally electronegative: $+5.28$ mV for DPAP-MgO₁ and 0 mV for DPAP-MgO₂. The net positive surface charge of DPAP-MgO₁ denotes its closeness to neutral stability, which is induced by molecular intercalation between the aptamer molecules, and highly electropositive and hydrophilic PEI particles. Further, it can be noted that the DPAP-MgO₂ sample was neutrally stable at pH 7. In our previous studies, we have also evaluated that these nanoparticles are stable for 43 days, which is efficient for effective drug release applications [26,45]. These neutral or close to neutral surface charged particles are highly beneficial for delivering the drug load with less accumulation and longer circulation lifetime in mononuclear phagocyte system [46–48]. Besides co-shielding and protecting the integrity of the encapsulated MgO₁ and MgO₂ nanodrug molecules, PEI intercalation with DNA aptamer molecules protects the functionality and bioactivity of the aptamer from nuclease attacks, systemic clearance, and cell membrane repulsion from the targeted cells. The zeta potential of DPAP-MgO₂ formulation was neutral. It is ideal to achieve DPAP formulation with an overall zeta potential of positive, neutral or slightly negative, in order to significantly minimize the strong electrostatic repulsive forces between the anionic payloads (MgO nanoparticles and aptamer molecules), and the negatively charged surface membrane of targeted cells in order to promote cell penetration, cellular uptake, and cell transfection.

3.3. Determination of loading capacity and encapsulation efficiency of DPAP-MgO₁ and DPAP-MgO₂ particulate systems

Table 2 shows the loading capacity and encapsulation efficiency comparisons between the DPAP-MgO₁ and DPAP-MgO₂ formulations. The MgO₁ nanoparticles were encapsulated within the PLGA polymeric

core, with a loading capacity of 0.008 mg/mg PLGA, and an encapsulation efficiency of 60.14% ; whilst the MgO₂ nanoparticles registered a loading capacity of 0.031 mg/mg PLGA, and an encapsulation efficiency of 93.69% . The significantly higher encapsulation efficiency of the biosynthesised MgO nanoparticles (MgO₂) could be due to an enhanced bio-complexation of MgO₂ nanoparticles into the biodegradable PLGA polymeric particles, potentially facilitated by the residual bioactive compounds, such as flavonoids accompanying the plant-leaf extract. The encapsulation efficiencies are either highly comparable, or higher than others reported in the literature for functional polymeric delivery devices. For example, paclitaxel-loaded PLGA particles [49], and paclitaxel-loaded aptamer-coupled PEG-PLGA nanocarriers [1], showed an encapsulation efficiency of 44.7% ; AS1411 aptamer-linked paclitaxel-carried PLGA-lecithin-PEG nanoparticles showed an encapsulation efficiency of 60.76% [9]; and EpCAM aptamer-conjugated PEG-PLGA formulation showed 91.25% encapsulation efficiency [41]. The DPAP-MgO₂ particulate system also demonstrated a more efficient coupling of aptamer molecules at an efficiency of 60.3% . The aptamer loading efficiency is in the same range of past reported findings. DNA-conjugated POE-PEI formulation showed approximately 65% [50]; and AS1411-linked drug-polymeric formulations showed 60.76% [51] and 44.7% [1] aptamer encapsulation efficiencies.

The DLS data demonstrate the potential of DPAP formulation in protecting the loaded aptamer molecules, via intercalation between the aptamer molecules and cationic PEI, to form a stable PEI-Aptamer polyplex. As a consequence, the aptamer and its functionality as the targeting ligand, could be preserved and protected from rapid glomerular filtration, nuclease-catalysed degradation and phagocytosis. The co-polymer characteristic of the DPAP particulate system allows a controlled and sustained release of the encapsulated drug molecules over a desired period. This could be attributed to the hydrolytic degradation mechanisms of both PEI and PLGA polymeric layers [44], under changing pH conditions during the targeted cellular events.

3.4. DNS assay of DPAP-MgO particles

DNS assay is a colorimetric quantification method based on DNS reaction, with reducing sugars or molecules containing the free carbonyl group. Aldehyde and ketone functional groups, which are present in the reducing sugars, undergo oxidation to form the carboxyl group. Consequently, DNS is reduced to 3-amino, 5-nitrosalicylic acid, which absorbs light at the wavelength of 540 nm, to produce a dark brown colored compound. It is commonly applied to determine the amount of carbohydrate present in biological samples. In the current study, 400 μ l/ml of DPAP-MgO₁ and DPAP-MgO₂ microparticles were incubated with 3T3 L1 cells in the presence of DNS reagent 25 h. A mixture of 3T3 L1 cells and DNS reagent (without the DPAP-MgO formulations) was used as the control. The concentration of glucose present in the DMEM medium was analysed after every 5 h to investigate the glucose uptake by 3T3 L1 cells and insulin resistance reversal.

The experimental data shown in Table 3 and Fig. 6 demonstrate the potential of both DPAP-MgO₁ and DPAP-MgO₂ formulations to lower the concentration of reducing sugars. The optical density (OD) decreased over the incubation duration, for both formulations. The color intensity is directly proportional to the concentration of reducing sugars available in the sample solution, as displayed in Fig. 5. This data also

Table 2

The average loading capacity and encapsulation efficiency of DPAP formulation carrying MgO nanoparticles.

Type of particulate delivery system	Loading capacity (mg MgO/mg PLGA)	Encapsulation efficiency in entrapping MgO (%)	Encapsulation efficiency in entrapping aptamer molecules (%)
DPAP-MgO ₁	0.00802	60.14	50.22
DPAP-MgO ₂	0.03100	93.69	60.30

Table 3

Summary of DNS assay data for both DPAP-MgO₁ and DPAP-MgO₂ formulations using 3T3 L1 cell lines at different time intervals. The numbers '1' and '2' within parenthesis in the 'Sample' column denote the first and second observation, respectively. Abbreviations: 'OD': Optical Density, 'Conc.': concentration. The mean of the two observations are shown in Fig. 6.

Sample	0 th hr		5th hr		10th hr		15th hr		20th hr		25th hr	
	OD	Conc. (μg/ml)	OD	Conc. (μg/ml)	OD	Conc. (μg/ml)	OD	Conc. (μg/ml)	OD	Conc. (μg/ml)	OD	Conc. (μg/ml)
Control [1]	1.790	3.500	1.720	3.300	1.680	3.200	1.560	3.000	1.470	2.800	0.340	0.700
Control [2]	1.760	3.400	1.700	3.250	1.690	3.250	1.590	3.050	1.500	2.900	0.270	0.550
DPAP-MgO ₁ [1]	1.440	2.750	1.400	2.700	1.360	2.600	1.300	2.500	1.280	2.450	0.006	0.030
DPAP-MgO ₁ [2]	1.400	2.700	1.390	2.650	1.350	2.600	1.280	2.450	1.260	2.400	0.006	0.030
DPAP-MgO ₂ [1]	1.380	2.650	1.360	2.600	1.340	2.550	1.300	2.500	1.270	2.450	0.007	0.040
DPAP-MgO ₂ [2]	1.390	2.700	1.340	2.550	1.320	2.500	1.310	2.500	1.290	2.500	0.008	0.040

shows that the DPAP formulation, carrying either MgO₁ or MgO₂ nanodrug particles, is capable of enhancing the targeting capability and the transfection efficiency towards targeted 3T3 L1 cells, to reverse insulin resistance. The presence of thrombin in the incubation medium, is anticipated to induce affinity molecular attachments to the 3T3 L1 cell membrane, creating artificial receptors, which improve DPAP interactions with the target cells. Table 3 shows a significant reduction in the concentrations of DPAP-MgO₁ and DPAP-MgO₂ supernatant samples after 25 h compared to the control samples. This indicates that the DPAP formulations are capable of directing MgO nanoparticles, to inhibit the oxidation of reducing sugars within 3T3 L1 cells, via an improved transfection efficiency.

It may be noted from Fig. 6 that the DPAP-MgO particulate system binds with the 3T3-L1 cells, due to the presence of thrombin, which

creates artificial receptors. The binding via thrombin based artificial receptors leads to a controlled release of MgO nanoparticles into the 3T3-L1 cells. The MgO nanoparticles enter the cells and dissociates into Mg²⁺ and O²⁻ ions, where the magnesium ions activate certain intracellular enzymes, such as poly (ADP-Ribose) synthetase [52]. The oxygen ion leads to the formation of intracellular reactive oxygen species, and causes cell death. This in turn promotes insulin reversal, resulting in a gradual increase in the extracellular glucose uptake. The enhanced reversal of insulin resistance allows more glucose to enter into the cells, which reduces the extracellular glucose, compared to the control. This demonstrates that the DPAP-MgO particulate system increases extracellular glucose uptake by reversing insulin resistance. Fig. 7 shows the mechanism of DPAP-MgO particulate system in increasing glucose uptake, in a diabetic cell model.

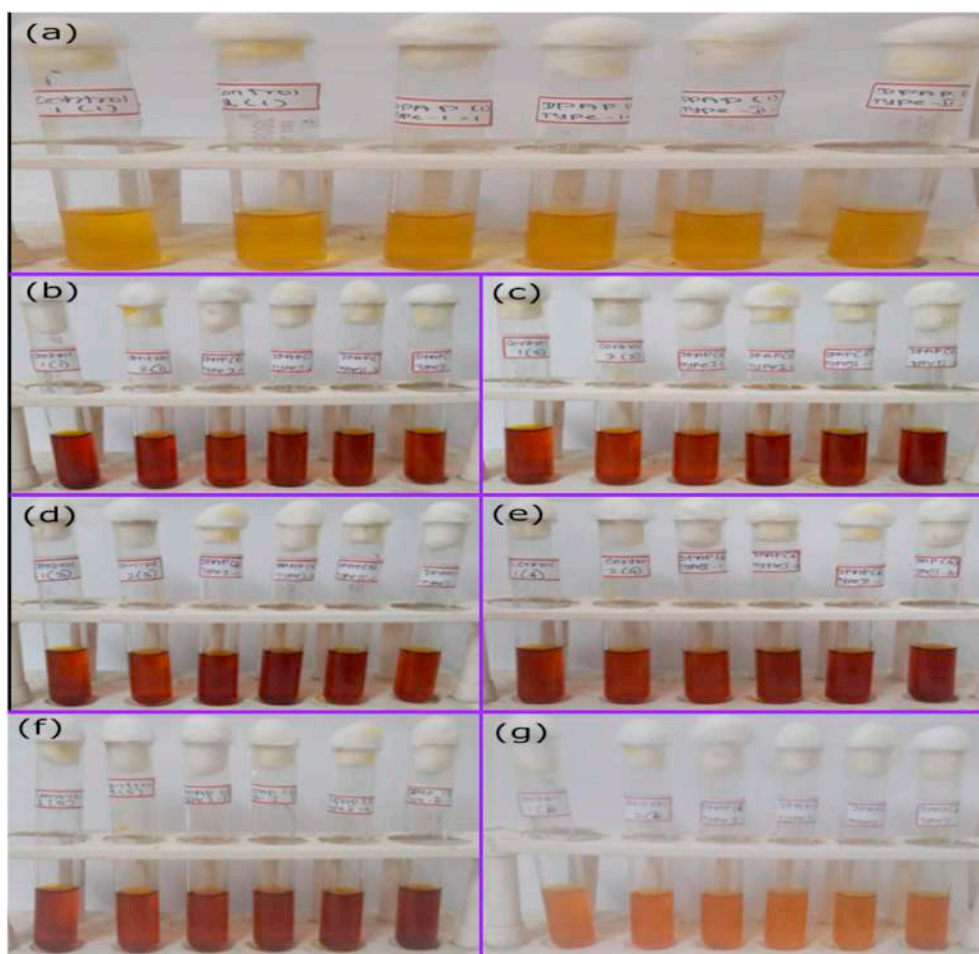


Fig. 5. Observed changes in DNS color intensity, for DPAP-MgO₁ and DPAP-MgO₂ supernatants, over a 25 h-incubation with 3T3 L1 cells. (For interpretation of the references to color in this figure legend, the reader is referred to the Web version of this article.)

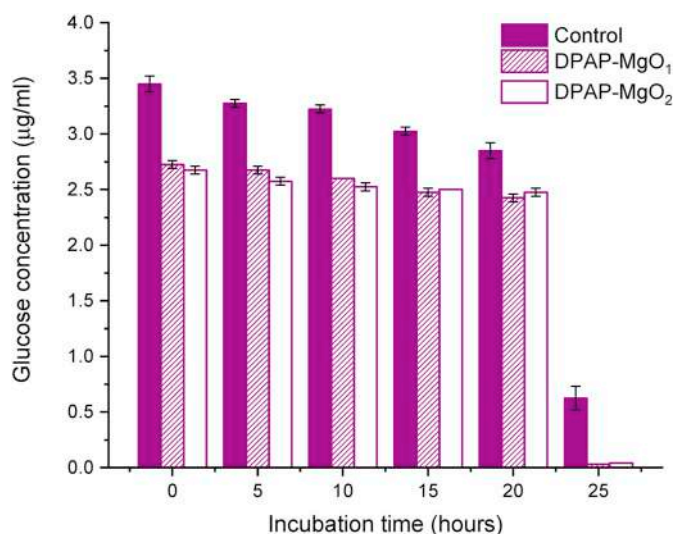


Fig. 6. DNS glucose concentrations ($\mu\text{g/ml}$) determined for DPAP-MgO₁ and DPAP-MgO₂, over a 25 h-incubation with 3T3 L1 cells.

The targeted binding and release of DPAP-MgO nanoformulation can be attributed to some engineered biophysical characteristics of the DPAP formulation, to facilitate effective cell transfection and delivery of intact drug molecules, to targeted 3T3 cells via aptamer navigation. The data from the DNS assay show that both MgO₁ and MgO₂ nano-drugs offer similar therapeutic efficacy, in inhibiting the oxidation of reducing sugars, indicating their extraordinary potential in controlling diabetes, hyperlipidemia, and obesity.

In the present work, the drug candidates used are MgO

nanoparticles, which possess the insulin resistance reversal capability, showing their promising potential in enhancing the Type 2 diabetic therapies. Therefore, the diabetic 3T3L1 cell line was selected over other cell lines in order to preliminarily demonstrate the targeting performance of the MgO-loaded aptamer-navigated DPAP system. This is mainly because of the fact that the 3T3L1 mouse cell line is a well-known and well-established pre-adipose cell line derived from the murine swiss 3T3 cells [53]. 3T3L1 cell lines, which could be differentiated into adipocytes, serve as excellent *in vitro* models to study and understand the glucose metabolism, due to their enhanced insulin sensitivity [54]. Moreover, most of the recently published works have also demonstrated the use of 3T3L1 cells for investigating diabetes and obesity-related characteristics [55–59]. 3T3 cell line is ideal for preliminary *in vitro* study, as it is easier and comparatively inexpensive to obtain, as well as generating a homogenous response to experiments and therapeutic treatments [54,60]. Accordingly, 3T3 cell line is sufficient to design a preliminary study, investigating the targeting capabilities of the MgO-DPAP system. In addition, both chemical and biosynthesised MgO nanoparticles are proven to be less toxic towards the 3T3L1 cell lines in our previous works [61,62]. Further, PLGA and PEI are common biocompatible polymers for nanoparticle delivery, that are non/less toxic towards various cells, as suggested in several previous literatures [63–66]. Furthermore, DPAP system with PLGA and PEI was also proven to be less toxic towards V79-4 lung cells in our previous study [67]. Thus, it is evident that the polymeric system will be less toxic towards mammalian cells and its efficient controlled drug delivery efficacy and neutral stability will prevent agglomeration of nanoparticles, which eventually will mitigate its toxic reactions. Nonetheless, future works can be carried out with other cell lines with validated control cell lines in order to further confirm the efficiency of co-polymeric DPAP system in term of cytotoxicity, targeting capability and delivery pattern.

1. Binding of DPAP-MgO particulate system with 3T3-L1 diabetic cell model

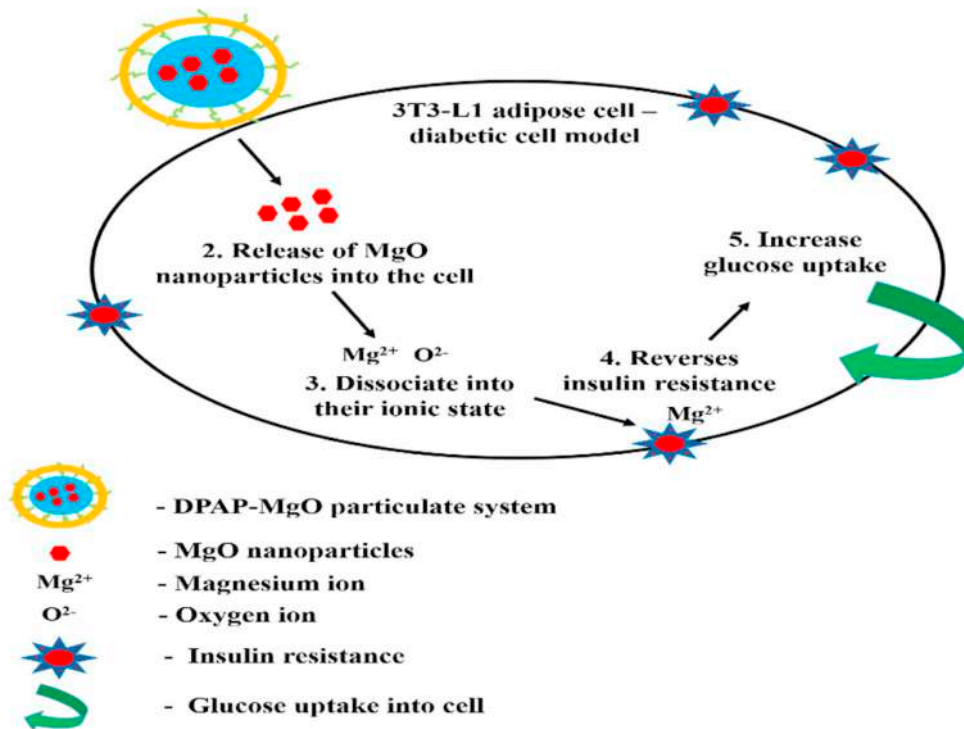


Fig. 7. Proposed mechanism for the DPAP-MgO targeted delivery and insulin resistance reversal in 3T3-L1 adipose cell lines.

4. Conclusions

The current study reports the synthesis of two types of DPAP formulations: DPAP-MgO₁ and DPAP-MgO₂, using a w/o/w double emulsion and ultra-sonication technique. Biophysical analysis of the formulations indicated that both DPAP-MgO₁ and DPAP-MgO₂ particulate systems possessed zeta potentials of +5.28 mV and +9.07 mV respectively, being desirable to enhance electrostatic interactions and endocytosis of MgO nanodrugs into the targeted cells. The encapsulation efficiency and loading capacity of DPAP-MgO₂ (DPAP with bio-synthesised MgO) formulation were 0.031 mg/mg PLGA and 93.69%, significantly higher than those of DPAP-MgO₁ (DPAP with chemically synthesized MgO) formulation. DNS assay indicated the efficacies of both DPAP-MgO₁ and DPAP-MgO₂ particulate systems in delivering MgO nanoparticles to the targeted 3T3 L1 cells through enhanced endocytosis and cellular transfection. As a result, the oxidation of reducing sugars within the 3T3 L1 cells was reduced, showing a promise for applications in the treatment of Type 2 diabetes. Aptamer-navigated DPAP copolymeric formulation represents a smart targeted drug carrier capable of delivering adequate amounts of MgO nanoparticles, which is sufficient to elicit effective *in vitro* therapies at target sites. The current *in vitro* study is preliminary, but crucial to demonstrate the successful delivery of MgO nanoparticles to the targeted 3T3-L1 diabetic cells, and resulted in the insulin resistance reversal ability. Notwithstanding, further *in vivo* studies are vital in cells and mouse models, to completely characterize the performance and effectiveness of MgO-loaded aptamer-navigated DPAP system in targeting and treating Type 2 diabetic cells. Also, more *in vivo* studies involving the DPAP-MgO particulate systems are mandatory in order to demonstrate complete preclinical efficacy in mammalian host systems.

Data availability

All results or data generated during this study are included in this article.

CRedit authorship contribution statement

Kei X. Tan: Investigation, Methodology, Visualization, Writing - original draft. **Jaison Jeevanandam:** Investigation, Methodology, Visualization, Writing - original draft. **Sharadwata Pan:** Writing - review & editing. **Lau Sie Yon:** Conceptualization, Supervision. **Michael K. Danquah:** Conceptualization, Methodology, Project administration, Funding acquisition, Resources, Supervision, Writing - original draft.

Declaration of competing interest

The authors declare that they have no financial or any other competing interests.

Funding and Acknowledgements

The current study was financially supported by the Ministry of Higher Education Malaysia through the Fundamental Research Grant Scheme (FRGS) - FRGS/1/2014/SKK07/CURTIN/02/1. The authors wish to acknowledge Life Teck Research Centre for their support with the cell line studies.

References

- [1] J. Guo, X. Gao, L. Su, H. Xia, G. Gu, Z. Pang, et al., Aptamer-functionalized PEG-PLGA nanoparticles for enhanced anti-glioma drug delivery, *Biomaterials* 32 (31) (2011) 8010–8020.
- [2] S. Senapati, A.K. Mahanta, S. Kumar, P. Maiti, Controlled drug delivery vehicles for cancer treatment and their performance, *Signal transduction and targeted therapy* 3 (1) (2018) 7.
- [3] M. Ye, J. Hu, M. Peng, J. Liu, J. Liu, H. Liu, et al., Generating aptamers by cell-SELEX for applications in molecular medicine, *Int. J. Mol. Sci.* 13 (3) (2012) 3341–3353.
- [4] W. Alshaer, H. Hillaireau, E. Fattal, Aptamer-guided nanomedicines for anticancer drug delivery, *Adv. Drug Deliv. Rev.* 134 (2018) 122–137, <https://doi.org/10.1016/j.addr.2018.09.011>.
- [5] K.X. Tan, M.K. Danquah, A. Sidhu, C.M. Ongkudon, S.Y. Lau, Towards targeted cancer therapy: aptamer or oncolytic virus? *Eur. J. Pharmaceut. Sci. : official journal of the European Federation for Pharmaceutical Sciences* 96 (2016) 8–19.
- [6] P. Sundaram, H. Kurniawan, M.E. Byrne, J. Wower, Therapeutic RNA aptamers in clinical trials, *Eur. J. Pharmaceut. Sci.* 48 (1–2) (2013) 259–271.
- [7] B.C. Wengert, J.A. Katakowski, J.M. Rosenberg, C.G. Park, S.C. Almo, D. Palliser, et al., Aptamer-targeted Antigen delivery, *Mol. Ther.* 22 (7) (2014) 1375–1387.
- [8] H. Sun, X. Zhu, P.Y. Lu, R.R. Rosato, W. Tan, Y. Zu, Oligonucleotide aptamers: new tools for targeted cancer therapy, *Mol. Ther.* 3 (2014) e182.
- [9] A. Aravind, P. Jeyamohan, R. Nair, S. Veerananayanan, Y. Nagaoka, Y. Yoshida, et al., AS1411 aptamer tagged PLGA-lecithin-PEG nanoparticles for tumor cell targeting and drug delivery, *Biotechnol. Bioeng.* 109 (11) (2012) 2920–2931.
- [10] F. Ghahremani, A. Kefayat, D. Shabbazi-Gahremani, H. Motaghi, M.A. Mehrgardi, S. Haghighi-Javanmard, AS1411 aptamer-targeted gold nanoclusters effect on the enhancement of radiation therapy efficacy in breast tumor-bearing mice, *Nanomedicine* 13 (20) (2018) 2563–2578.
- [11] N. Subramanian, J. Kanwar, P. Athalya, N. Janakiraman, V. Khetan, R. Kanwar, et al., EpCAM aptamer mediated cancer cell specific delivery of EpCAM siRNA using polymeric nanocomplex, *J. Biomed. Sci.* 22 (1) (2015) 4.
- [12] K. Min, H. Jo, K. Song, M. Cho, Y.-S. Chun, S. Jon, et al., Dual-aptamer-based delivery vehicle of doxorubicin to both PSMA (+) and PSMA (–) prostate cancers, *Biomaterials* 32 (8) (2011) 2124–2132.
- [13] F. He, N. Wen, D. Xiao, J. Yan, H. Xiong, S. Cai, et al., Aptamer-based targeted drug delivery systems: current potential and challenges, *Curr. Med. Chem.* (2018), <https://doi.org/10.2174/0929867325666181008142831>.
- [14] M. de Lores Lima, T. Cruz, J.C. Pousada, L.E. Rodrigues, K. Barbosa, V. Cangucu, The effect of magnesium supplementation in increasing doses on the control of type 2 diabetes, *Diabetes Care* 21 (5) (1998) 682–686.
- [15] L.A. Olatunji, A.O. Soladoye, Increased magnesium intake prevents hyperlipidemia and insulin resistance and reduces lipid peroxidation in fructose-fed rats, *Pathophysiology : the official journal of the International Society for Pathophysiology* 14 (1) (2007) 11–15.
- [16] P. Connes, S. Dufour, A. Pichon, F. Favre, Blood Rheology, Blood Flow, and Human Health. Nutrition and Enhanced Sports Performance, Elsevier, 2019, pp. 359–369.
- [17] F. Guerrero-Romero, M. Rodriguez-Moran, Complementary therapies for diabetes: the case for chromium, magnesium, and antioxidants, *Arch. Med. Res.* 36 (3) (2005) 250–257.
- [18] S. Sohrabipour, M.R. Sharifi, M. Sharifi, A. Talebi, N. Soltani, Effect of magnesium sulfate administration to improve insulin resistance in type 2 diabetes animal model: using the hyperinsulinemic-euglycemic clamp technique, *Fundamental & clinical pharmacology* 32 (6) (2018) 603–616.
- [19] N. Naghsh, S. Kazemi, Effect of nano-magnesium oxide on glucose concentration and lipid profile in diabetic laboratory mice, *Iran. J. Pharm. Sci.* 10 (3) (2014) 63–68.
- [20] L. Jahangiri, M. Kesmati, H. Najafzadeh, Evaluation of anticonvulsive effect of magnesium oxide nanoparticles in comparison with conventional MgO in diabetic and non-diabetic male mice, *Basic Clin. Neurosci.* 5 (2) (2014) 156–161.
- [21] S. Moeini-Nodeh, M. Rahimifard, M. Baeeri, M. Abdollahi, Functional improvement in rats' pancreatic islets using magnesium oxide nanoparticles through antiapoptotic and antioxidant pathways, *Biol. Trace Elem. Res.* 175 (1) (2017) 146–155.
- [22] M. Kesmati, M. Torabi, H. Teymuri Zamaneh, H. Malekshahi Nia, Interaction between anxiolytic effects of magnesium oxide nanoparticles and exercise in adult male rat, *Nanomedicine Journal* 1 (5) (2014) 324–330.
- [23] I.F. Alexa, M. Ignat, R.F. Popovici, D. Timpu, E. Popovici, In vitro controlled release of antihypertensive drugs intercalated into unmodified SBA-15 and MgO modified SBA-15 matrices, *International journal of pharmaceuticals* 436 (1–2) (2012) 111–119.
- [24] V. Heydari, M. Navaei-Nigeh, M. Rahimifard, A. Mohammadirad, M. Baeeri, M. Abdollahi, Biochemical and molecular evidences on the protection by magnesium oxide nanoparticles of chlorpyrifos-induced apoptosis in human lymphocytes, *J. Res. Med. Sci. : The Official Journal of Isfahan University of Medical Sciences* 20 (11) (2015) 1021–1031.
- [25] J. Jeevanandam, Enhanced Synthesis and Delivery of Magnesium Oxide Nanoparticles for Reverse Insulin Resistance in Type 2 Diabetes Mellitus, (2017).
- [26] K.X. Tan, M.K. Danquah, A. Sidhu, S.Y. Lau, C.M. Ongkudon, Biophysical characterization of layer-by-layer synthesis of aptamer-drug microparticles for enhanced cell targeting, *Biotechnol. Prog.* 34 (1) (2018) 249–261.
- [27] K.X. Tan, M.K. Danquah, A. Sidhu, S.Y. Lau, C.M. Ongkudon, Biophysical characterization of layer-by-layer synthesis of aptamer-drug microparticles for enhanced cell targeting, *Biotechnol. Prog.* 34 (2017) 249–261.
- [28] K.X. Tan, S.Y. Lau, M.K. Danquah, Process evaluation and in vitro selectivity analysis of aptamer-drug polymeric formulation for targeted pharmaceutical delivery, *Biomed. Pharmacother.* 101 (2018) 996–1002.
- [29] V. Gulati, P. Gulati, I.H. Harding, E.A. Palombo, Exploring the anti-diabetic potential of Australian Aboriginal and Indian Ayurvedic plant extracts using cell-based assays, *BMC Compl. Alternative Med.* 15 (2015) 8.
- [30] B.D. Kumar, K. Krishnakumar, S.K. Jaganathan, M. Mandal, Effect nimbine on glucose utilization in 3T3-L1 cells, *Phcog. Mag.* 9 (33) (2013) 72–75.
- [31] F.J. Ruiz-Ojeda, A.I. Ruperez, C. Gomez-Llorente, A. Gil, C.M. Aguilera, Cell models and their application for studying adipogenic differentiation in relation to obesity: a review, *Int. J. Mol. Sci.* 17 (7) (2016) 1040.

- [32] J. Jeevanandam, Y.S. Chan, M.K. Danquah, Calcination-dependent morphology transformation of sol-gel-synthesized MgO nanoparticles, *Chemistry select* 2 (32) (2017) 10393–10404.
- [33] J. Jeevanandam, Y.S. Chan, M.K. Danquah, Biosynthesis and characterization of MgO nanoparticles from plant extracts via induced molecular nucleation, *New J. Chem.* 41 (7) (2017) 2800–2814.
- [34] Q. Yi, J. Ma, K. Kang, Z. Gu, Dual cellular stimuli-responsive hydrogel nanocapsules for delivery of anticancer drugs, *J. Mater. Chem. B* 4 (28) (2016) 4922–4933.
- [35] J. Jeevanandam, Y.S. Chan, M.K. Danquah, Calcination-dependent morphology transformation of sol-gel-synthesized MgO nanoparticles, *ChemistrySelect* 2 (32) (2017) 10393–10404.
- [36] Rashid M. Nidhi, V. Kaur, S.S. Hallan, S. Sharma, N. Mishra, Microparticles as controlled drug delivery carrier for the treatment of ulcerative colitis: a brief review, *Saudi Pharmaceut. J.* 24 (4) (2016) 458–472.
- [37] T.A. Ahmed, B.M. Aljaeid, Preparation, characterization, and potential application of chitosan, chitosan derivatives, and chitosan metal nanoparticles in pharmaceutical drug delivery, *Drug Des. Dev. Ther.* 10 (2016) 483–507.
- [38] S. Trows, R. Scherließ, Carrier-based dry powder formulation for nasal delivery of vaccines utilizing BSA as model drug, *Powder Technol.* 292 (2016) 223–231.
- [39] L. Caetano, A. Almeida, L. Gonçalves, Effect of experimental parameters on alginate/chitosan microparticles for BCG encapsulation, *Mar. Drugs* 14 (5) (2016) 90.
- [40] P. Pacheco, D. White, T. Sulchek, Effects of microparticle size and Fe density on macrophage phagocytosis, *PLoS One* 8 (4) (2013) e60989.
- [41] M. Alibolandi, M. Ramezani, F. Sadeghi, K. Abnous, F. Hadizadeh, Epithelial cell adhesion molecule aptamer conjugated PEG–PLGA nanopolymerosomes for targeted delivery of doxorubicin to human breast adenocarcinoma cell line in vitro, *International journal of pharmaceutics* 479 (1) (2015) 241–251.
- [42] M.V. Balashanmugam, S. Nagarethinam, H. Jagani, V.R. Josyula, A. Alrohaime, N. Udupa, Preparation and characterization of novel PBAE/PLGA polymer blend microparticles for DNA vaccine delivery, *The Scientific World Journal* 2014 (2014) 385135.
- [43] M. Obulesu, Chapter 9 - nanoparticles: the double-edged swords, in: M. Obulesu (Ed.), *Alzheimer's Disease Theranostics*, Academic Press, 2019, pp. 51–57.
- [44] Y.S. Hii, J. Jeevanandam, Y.S. Chan, Plant mediated green synthesis and nanoencapsulation of MgO nanoparticle from *Calotropis gigantea*: Characterisation and kinetic release studies, *Inorganic and Nano-Metal Chemistry* 48 (12) (2018) 620–631.
- [45] K.X. Tan, M.K. Danquah, S. Pan, L.S. Yon, Binding characterization of aptamer-drug layered microformulations and in vitro release assessment, *J. Pharmaceut. Sci.* 108 (9) (2019) 2934–2941.
- [46] K. Xiao, Y. Li, J. Luo, J.S. Lee, W. Xiao, A.M. Gonik, et al., The effect of surface charge on in vivo biodistribution of PEG-oligocholeic acid based micellar nanoparticles, *Biomaterials* 32 (13) (2011) 3435–3446.
- [47] E. Blanco, H. Shen, M. Ferrari, Principles of nanoparticle design for overcoming biological barriers to drug delivery, *Nat. Biotechnol.* 33 (9) (2015) 941.
- [48] J. Jeevanandam, Y.S. Chan, M.K. Danquah, Calcination-dependent morphology transformation of sol-gel-synthesized MgO nanoparticles, *ChemistrySelect* 2 (32) (2017) 10393–10404.
- [49] N. Sharma, P. Madan, S. Lin, Effect of process and formulation variables on the preparation of parenteral paclitaxel-loaded biodegradable polymeric nanoparticles: a co-surfactant study, *Asian J. Pharm. Sci.* 11 (3) (2016) 404–416.
- [50] D.N. Nguyen, S.S. Raghavan, L.M. Tashima, E.C. Lin, S.J. Fredette, R.S. Langer, et al., Enhancement of poly(orthoester) microspheres for DNA vaccine delivery by blending with poly(ethylenimine), *Biomaterials* 29 (18) (2008) 2783–2793.
- [51] A. Aravind, S.H. Varghese, S. Veeranarayanan, A. Mathew, Y. Nagaoka, S. Iwai, et al., Aptamer-labeled PLGA nanoparticles for targeting cancer cells, *Cancer Nanotechnology* 3 (1–6) (2012) 1–12.
- [52] X. Luo, K.W. Ryu, D.-S. Kim, T. Nandu, C.J. Medina, R. Gupta, et al., PARP-1 controls the adipogenic transcriptional program by PARYlating C/EBP β and modulating its transcriptional activity, *Molecular cell* 65 (2) (2017) 260–271.
- [53] F.J. Ruiz-Ojeda, A.I. Ruperez, C. Gomez-Llorente, A. Gil, C.M. Aguilera, Cell models and their application for studying adipogenic differentiation in relation to obesity: a review, *Int. J. Mol. Sci.* 17 (7) (2016).
- [54] D. Vishwanath, H. Srinivasan, M.S. Patil, S. Seetarama, S.K. Agrawal, M.N. Dixit, et al., Novel method to differentiate 3T3 L1 cells in vitro to produce highly sensitive adipocytes for a GLUT4 mediated glucose uptake using fluorescent glucose analog, *Journal of cell communication and signaling* 7 (2) (2013) 129–140.
- [55] Y.-L. Chow, Y. Iwata, F. Sato, Dihydroanguinarine enhances glucose uptake in mouse 3T3-L1 cells, *ACS Omega* 2 (10) (2017) 6916–6925.
- [56] D. Chen, Y. Wang, K. Wu, X. Wang, Dual effects of metformin on adipogenic differentiation of 3T3-L1 preadipocyte in AMPK-dependent and independent manners, *Int. J. Mol. Sci.* 19 (6) (2018) 1547.
- [57] M.-M. Marisol, T.-M. Celeste, M.-M. Laura, E.-G. Fernando, P.-C. José, Z. Alejandro, et al., Effect of cucumis sativus on dysfunctional 3T3-L1 adipocytes, *Sci. Rep.* 9 (1) (2019) 13372.
- [58] V.P. Knutson, B. Yvonne, 3T3-L1 adipocytes as a cell culture model of insulin resistance, *Vitro Cellular & Developmental Biology Animal*, vol. 33, 1997, pp. 77–81.
- [59] S. Al-Shaeli, A. Ethaeb, J. Brown, Abundant active ingredients of green tea regulate glucose metabolism in 3T3-L1 cell line, *Indian Journal of Forensic Medicine & Toxicology* 13 (2019) 738.
- [60] K. Zebisch, V. Voigt, M. Wabitsch, M. Brandsch, Protocol for effective differentiation of 3T3-L1 cells to adipocytes, *Anal. Biochem.* 425 (1) (2012) 88–90.
- [61] J. Jeevanandam, Y. San Chan, M.K. Danquah, M.C. Law, Cytotoxicity analysis of morphologically different sol-gel-synthesized MgO nanoparticles and their in vitro insulin resistance reversal ability in adipose cells, *Applied biochemistry and biotechnology* (2019) 1–26.
- [62] J. Jeevanandam, Enhanced Synthesis and Delivery of Magnesium Oxide Nanoparticles for Reverse Insulin Resistance in Type 2 Diabetes Mellitus, *Curtin University*, 2017.
- [63] Z.-C. Xing, W.-P. Chae, M.-W. Huh, L.-S. Park, S.-Y. Park, G. Kwak, et al., In vitro anti-bacterial and cytotoxic properties of silver-containing poly (L-lactide-co-glycolide) nanofibrous scaffolds, *J. Nanosci. Nanotechnol.* 11 (1) (2011) 61–65.
- [64] C.M. Moraes, A.P. de Matos, R. de Lima, A.H. Rosa, E. de Paula, L.F. Fraceto, Initial development and characterization of PLGA nanospheres containing ropivacaine, *J. Biol. Phys.* 33 (5–6) (2007) 455.
- [65] W. Dong, S. Li, G. Jin, Q. Sun, D. Ma, Z. Hua, Efficient gene transfection into mammalian cells mediated by cross-linked polyethylenimine, *Int. J. Mol. Sci.* 8 (2) (2007) 81–102.
- [66] M. Havrdova, K. Hola, J. Skopalik, K. Tomankova, M. Petr, K. Cepe, et al., Toxicity of carbon dots—Effect of surface functionalization on the cell viability, reactive oxygen species generation and cell cycle, *Carbon* 99 (2016) 238–248.
- [67] K.X. Tan, M.K. Danquah, A. Sidhu, S.Y. Lau, C.M. Ongkudon, Biophysical characterization of layer-by-layer synthesis of aptamer-drug microparticles for enhanced cell targeting, *Biotechnol. Prog.* 34 (1) (2018) 249–261.